

PREPARED FOR SUBMISSION TO JHEP

# Reassessing CP Violation in the C2HDM with Machine Learning

---

Rafael Boto <sup>a</sup>, Karim Elyauti <sup>a</sup>, Duarte Fontes <sup>a</sup>, Maria Gonçalves <sup>a,b</sup>,  
Margarete Mühlleitner <sup>a</sup>, Jorge C. Romão <sup>c</sup>, Rui Santos <sup>b,d</sup> and João P. Silva <sup>c</sup>

<sup>a</sup>*Institute for Theoretical Physics, Karlsruhe Institute of Technology,  
76128 Karlsruhe, Germany*

<sup>b</sup>*Centro de Física Teórica e Computacional, Faculdade de Ciências,  
Universidade de Lisboa, Campo Grande, Edifício C8, 1749-016 Lisboa, Portugal*

<sup>c</sup>*Departamento de Física and CFTP, Instituto Superior Técnico, Universidade de Lisboa,  
Avenida Rovisco Pais 1, 1049-001 Lisboa, Portugal*

<sup>d</sup>*ISEL - Instituto Superior de Engenharia de Lisboa,  
Instituto Politécnico de Lisboa 1959-007 Lisboa, Portugal*

*E-mail:* [rafael.boto@kit.edu](mailto:rafael.boto@kit.edu), [karim.elyauti@partner.kit.edu](mailto:karim.elyauti@partner.kit.edu),  
[duarte.fontes@kit.edu](mailto:duarte.fontes@kit.edu), [magoncalves@fc.ul.pt](mailto:magoncalves@fc.ul.pt),  
[margarete.muehlleitner@kit.edu](mailto:margarete.muehlleitner@kit.edu), [jorge.romao@tecnico.ulisboa.pt](mailto:jorge.romao@tecnico.ulisboa.pt),  
[rasantos@fc.ul.pt](mailto:rasantos@fc.ul.pt), [jpsilva@cftp.ist.utl.pt](mailto:jpsilva@cftp.ist.utl.pt)

**ABSTRACT:** We provide a study of the parameter space of the complex 2-Higgs Doublet Model (C2HDM), focusing on signs of large CP-violating couplings of the 125 GeV Higgs boson with the fermions. The study is performed utilizing Machine Learning (ML) techniques developed recently for parameter space exploration, including an Evolutionary Strategy Algorithm and Novelty Reward. We give particular attention to the electron electric dipole moment (eEDM). We confirm that the recently found kite diagrams are crucial for the outcome of the analysis. Moreover, their use also mitigates the dependence of the results on the scale and scheme choice of the masses in the loop diagrams. We furthermore point out that, already at the current level of experimental precision, the Barr-Zee diagrams with charm quark loops must be taken into account. The combined use of kite diagrams and ML techniques allows for the resurrection of large fermion CP-odd couplings for Type-II and Flipped C2HDM when the 125 GeV Higgs coincides with the second lightest neutral scalar. This arises due to cancellations, typically of the per-mil order, which, moreover, will still be possible for a foreseeable eEDM precision down to  $10^{-33}$  e.cm. For these cases, the constraints on the CP-odd couplings arises from the precision LHC measurements.

---

## Contents

<b>1</b>	<b>Introduction</b>	<b>1</b>
<b>2</b>	<b>The C2HDM</b>	<b>3</b>
<b>3</b>	<b>The electron EDM</b>	<b>6</b>
<b>4</b>	<b>Sampling</b>	<b>7</b>
4.1	Theoretical and experimental constraints	7
4.2	Sampling techniques	8
<b>5</b>	<b>Results for Type-II with <math>h_2 = h_{125}</math></b>	<b>9</b>
5.1	Phenomenology with Strategy 1	9
5.2	Phenomenology with Strategy 2	11
5.3	Isolated regions with small $h_1$ masses	13
5.4	The charm diagrams	14
<b>6</b>	<b>Revisiting other cases of the C2HDM</b>	<b>16</b>
<b>7</b>	<b>Conclusions</b>	<b>17</b>
<b>A</b>	<b><math>\chi^2</math> exclusion</b>	<b>19</b>

---

## 1 Introduction

T.D. Lee showed that a 2-Higgs Doublet Model (2HDM) allows for spontaneous CP violation in the scalar sector [1]. Experiments in  $B$ -physics [2, 3] guarantee that the CP violation in  $W$  boson interactions, predicted in the Standard Model (SM), must be large. This spurred interest in a more general CP-violating framework in the 2HDM. In order to avoid flavour-changing neutral scalar interactions, a  $\mathbb{Z}_2$  symmetry is usually employed [4, 5]. This leads to a CP-conserving scalar sector in the 2HDM and, moreover, precludes a decoupling limit. Both problems may be solved by introducing in the potential a complex soft-symmetry breaking term ( $m_{12}^2$ ). This leads to the complex 2HDM (C2HDM), which has been extensively explored in the literature; see, for example, Refs. [6–42].

Models with CP violation in the scalar sector must contend with potentially large contributions to the electron electric dipole moment (eEDM). The leading contributions arise from two-loop Barr-Zee diagrams [43] and extensions [44–46]. In Ref. [36] it was shown that a new class of two-loop diagrams (dubbed “kite diagrams”) is essential for the gauge independence of the final result. In a subsequent article, relevant one-loop diagrams were also identified [47].

The inclusion of all relevant diagrams in the computation of the eEDM is crucial for the following two reasons. On the one hand, current experiments are extremely accurate: the 90% confidence-level limit on the eEDM reported by the ACME collaboration is  $1.1 \times 10^{-29}$  e.cm [48–50], while JILA quotes  $4.1 \times 10^{-30}$  e.cm [50]. On the other hand, in the Feynman gauge, each individual diagram can typically yield values of order  $10^{-27}$  e.cm. Thus, in order to get substantial large CP violation (e.g. in Higgs-fermion vertices), there needs to be a substantial cancellation among different eEDM diagrams, often of one part per mil. This forces the consideration of previously overlooked diagrams; for example, we will show that, given the current eEDM constraints, Barr-Zee diagrams involving virtual charm quarks need to be included. The expected sensitivity of future eEDM experiments has been discussed to be  $\mathcal{O}(10^{-33})$  e.cm [51–53], increasing the difficulty of obtaining the necessary cancellations in a scenario of non-discovery. Using the diagrams included in our study, we show that the cancellations can still be met for different cases of C2HDM.

The impact of eEDM measurements on the C2HDM parameter space has been considered by a number of authors [22–29]. In Ref. [29], a subset of the authors of this work

Type	I	II	LS	Flipped
$h_1 = h_{125}$	×	×	$\tau$	<u>×</u>
$h_2 = h_{125}$	×	<u>×</u>	$\tau$	×
$h_3 = h_{125}$	×	×	$\tau$	×

**Table 1:** Results for the possibility of large Yukawa couplings from Ref. [29]. A cross means that it is not possible to have large CP-odd couplings, i.e.  $|c^o| \gtrsim |c^e|$ . The notation  $\tau$  means that  $c^o/c^e$  is limited by the direct searches for CP-violating angular correlations of tau leptons in  $h_{125} \rightarrow \tau\bar{\tau}$  decays [54]. Underlined crosses indicate a change from allowed ( $\checkmark$ ) to excluded ( $\times$ ) compared to the previous analysis carried out in 2017 [25].

revisited the C2HDM taking into account the then most recent experimental results in order to quantify the amount of CP-violation that was still possible in the coupling of the SM-like Higgs to the fermions. In the C2HDM, there are three neutral scalars with mixed CP nature, denoted by  $h_1$ ,  $h_2$ , and  $h_3$ , ordered by increasing masses. The Higgs particle found at Large Hadron Collider (LHC) with mass of 125 GeV [55, 56] is denoted by  $h_{125}$ . All three possibilities —  $h_1 = h_{125}$ ,  $h_2 = h_{125}$  and  $h_3 = h_{125}$  — have been considered. The CP-even (CP-odd)  $h_{125}ff$  couplings are denoted by  $c_f^e$  ( $c_f^o$ ), where  $f$  denotes a fermion. The analysis is performed for each of the four  $\mathbb{Z}_2$ -symmetric C2HDM submodels, namely, Type-I, Type-II, Lepton-Specific (LS) and Flipped. In Ref. [29], the particular case of the Type-II model with the configuration  $h_2 = h_{125}$  received special attention, for reasons detailed below. For reference, we display in Tab. 1 the results found in [29] on the possibility of a large CP-odd coupling admixture to the  $h_{125}$  Yukawa couplings. In this work, we revisit this table in light of the new scanning techniques.

Valid points in the C2HDM parameter space were found in Refs. [25, 29] by manually scanning close to the CP-conserving limit and iteratively enlarging the pseudoscalar component. This method was also followed for the  $\mathbb{Z}_2 \times \mathbb{Z}_2$  3HDM in Ref. [57]. Using a machine-learning (ML) algorithm with an Evolutionary Strategy and Novelty Reward

mechanism, it was shown in Ref. [58] that this method seriously misses valid regions of the model’s parameter space and the resulting physical implications. This motivated us to revisit the C2HDM with the same ML strategy. In particular, we found that the possibility of large CP-odd Higgs-fermion couplings for the Flipped Type with  $h_2 = h_{125}$ , which seemed impossible using the usual search techniques, is revived.

ML has become an essential tool in particle physics, driven by the increasing complexity and volume of data from experiments like those at the LHC. Recent reviews [59–61] include the developments in different fronts of Artificial Intelligence in high-energy physics. We are interested in the validation of a Beyond-the-SM (BSM) theory through constraints on its parameter space. Successful approaches to sampling the parameter space of BSMS have been developed in cases where training datasets are available [62–68]. Given the goal set on finding physical implications that we do not yet know about in highly constrained scans, we turn to search methods that do not rely on an initial set of sampled data. We consider an Evolutionary Strategy algorithm, first introduced in Ref. [69] to find valid and verifiable points of the model, combined with an anomaly detection used for Novelty Reward developed in Ref. [70], to ensure good exploration of parameter spaces and of the physical observables of the model.

The work is organized as follows. In Section 2, we recapitulate the symmetries and resulting Lagrangian for the C2HDM, with the possible model choices for the Yukawa couplings. In Section 3, we succinctly describe the status of the eEDM calculation in the C2HDM and the experimental bounds. In Section 4, we complete the list of constraints to be applied to this model, both theoretical and experimental ones, followed by the description of the adopted sampling strategy. Sections 5 and 6 are devoted our results, the former focused on the case Type-II with  $h_{125} = h_2$ , and the latter on other cases. After summarizing our conclusions in Section 7, we present the details of our application of `HiggsSignals` in Appendix A.

## 2 The C2HDM

In this work, we discuss an extension of the SM with a CP-violating scalar sector, with the addition of a scalar doublet with a softly broken  $\mathbb{Z}_2$  symmetry, known as the C2HDM [6–14]. We follow the description of the model in Ref. [25] and write the scalar potential as

$$\begin{aligned}
V = & m_{11}^2 |\Phi_1|^2 + m_{22}^2 |\Phi_2|^2 - \left( m_{12}^2 \Phi_1^\dagger \Phi_2 + h.c. \right) + \frac{\lambda_1}{2} (\Phi_1^\dagger \Phi_1)^2 + \frac{\lambda_2}{2} (\Phi_2^\dagger \Phi_2)^2 \\
& + \lambda_3 (\Phi_1^\dagger \Phi_1) (\Phi_2^\dagger \Phi_2) + \lambda_4 (\Phi_1^\dagger \Phi_2) (\Phi_2^\dagger \Phi_1) + \left[ \frac{\lambda_5}{2} (\Phi_1^\dagger \Phi_2)^2 + h.c. \right], \quad (2.1)
\end{aligned}$$

where all couplings are real, except for  $m_{12}^2$  and  $\lambda_5$ . Each of the doublets is written as an expansion around the real vacuum expectation values (vevs) of the neutral components  $\langle \Phi_i^0 \rangle = v_i / \sqrt{2}$  ( $i = 1, 2$ ), with  $v^2 = v_1^2 + v_2^2 \approx 246$  GeV,

$$\Phi_1 = \begin{pmatrix} \phi_1^+ \\ \frac{v_1 + \rho_1 + i\eta_1}{\sqrt{2}} \end{pmatrix} \quad \text{and} \quad \Phi_2 = \begin{pmatrix} \phi_2^+ \\ \frac{v_2 + \rho_2 + i\eta_2}{\sqrt{2}} \end{pmatrix}. \quad (2.2)$$

The minimum conditions can then be written as three equations,

$$m_{11}^2 v_1 + \frac{\lambda_1}{2} v_1^3 + \frac{\lambda_{345}}{2} v_1 v_2^2 = \text{Re}(m_{12}^2) v_2, \quad (2.3)$$

$$m_{22}^2 v_2 + \frac{\lambda_2}{2} v_2^3 + \frac{\lambda_{345}}{2} v_1^2 v_2 = \text{Re}(m_{12}^2) v_1, \quad (2.4)$$

$$2 \text{Im}(m_{12}^2) = v_1 v_2 \text{Im}(\lambda_5), \quad (2.5)$$

which, for non-zero vevs  $v_1$  and  $v_2$ , ensure one independent CP-violating phase if  $\text{Im}\left\{\lambda_5^* (m_{12}^2)^2\right\} \neq 0$  [6, 7, 11]. The diagonalization procedure starts with a rotation to the Higgs basis [71–74],

$$\begin{pmatrix} \mathcal{H}_1 \\ \mathcal{H}_2 \end{pmatrix} = R_H^T \begin{pmatrix} \Phi_1 \\ \Phi_2 \end{pmatrix} \equiv \begin{pmatrix} c_\beta & s_\beta \\ -s_\beta & c_\beta \end{pmatrix} \begin{pmatrix} \Phi_1 \\ \Phi_2 \end{pmatrix}, \quad (2.6)$$

with

$$\tan \beta \equiv \frac{v_2}{v_1}. \quad (2.7)$$

The doublets in the Higgs basis can then be written, with the Goldstone bosons  $G^\pm$  and  $G^0$  in  $\mathcal{H}_1$ , as

$$\mathcal{H}_1 = \begin{pmatrix} G^\pm \\ \frac{1}{\sqrt{2}}(v + H^0 + iG^0) \end{pmatrix} \quad \text{and} \quad \mathcal{H}_2 = \begin{pmatrix} H^\pm \\ \frac{1}{\sqrt{2}}(R_2 + iI_2) \end{pmatrix}. \quad (2.8)$$

The mass matrix for the neutral Higgs states is defined for  $\rho_1$ ,  $\rho_2$  and  $\rho_3 = I_2$  as,

$$(\mathcal{M}^2)_{ij} = \left\langle \frac{\partial^2 V}{\partial \rho_i \partial \rho_j} \right\rangle, \quad (2.9)$$

which can be diagonalized by a general orthogonal matrix  $R$  [15]. That is,

$$R \mathcal{M}^2 R^T = \text{diag}(m_1^2, m_2^2, m_3^2), \quad (2.10)$$

for which we follow the choice

$$R = \begin{pmatrix} c_1 c_2 & s_1 c_2 & s_2 \\ -(c_1 s_2 s_3 + s_1 c_3) & c_1 c_3 - s_1 s_2 s_3 & c_2 s_3 \\ -c_1 s_2 c_3 + s_1 s_3 & -(c_1 s_3 + s_1 s_2 c_3) & c_2 c_3 \end{pmatrix}, \quad (2.11)$$

with the notation  $s_i \equiv \sin \alpha_i$ ,  $c_i \equiv \cos \alpha_i$  ( $i = 1, 2, 3$ ), in the ranges

$$-\pi/2 < \alpha_1 \leq \pi/2, \quad -\pi/2 < \alpha_2 \leq \pi/2, \quad -\pi/2 < \alpha_3 \leq \pi/2. \quad (2.12)$$

The model contains three neutral particles with no definite CP quantum numbers,  $h_1$ ,  $h_2$  and  $h_3$ , and two charged scalars  $H^\pm$ . The masses for the neutral Higgs bosons are ordered such that  $m_1 \leq m_2 \leq m_3$ . The set of independent parameters of the potential sector can be chosen as

$$\tan \beta, m_{H^\pm}, \alpha_1, \alpha_2, \alpha_3, m_1, m_2, \text{Re}(m_{12}^2). \quad (2.13)$$

	up-type	down-type	leptons
Type-I	$\frac{R_{i2}}{s_\beta} - i\frac{R_{i3}}{t_\beta}\gamma_5$	$\frac{R_{i2}}{s_\beta} + i\frac{R_{i3}}{t_\beta}\gamma_5$	$\frac{R_{i2}}{s_\beta} + i\frac{R_{i3}}{t_\beta}\gamma_5$
Type-II	$\frac{R_{i2}}{s_\beta} - i\frac{R_{i3}}{t_\beta}\gamma_5$	$\frac{R_{i1}}{c_\beta} - it_\beta R_{i3}\gamma_5$	$\frac{R_{i1}}{c_\beta} - it_\beta R_{i3}\gamma_5$
Lepton-Specific	$\frac{R_{i2}}{s_\beta} - i\frac{R_{i3}}{t_\beta}\gamma_5$	$\frac{R_{i2}}{s_\beta} + i\frac{R_{i3}}{t_\beta}\gamma_5$	$\frac{R_{i1}}{c_\beta} - it_\beta R_{i3}\gamma_5$
Flipped	$\frac{R_{i2}}{s_\beta} - i\frac{R_{i3}}{t_\beta}\gamma_5$	$\frac{R_{i1}}{c_\beta} - it_\beta R_{i3}\gamma_5$	$\frac{R_{i2}}{s_\beta} + i\frac{R_{i3}}{t_\beta}\gamma_5$

**Table 2:** Yukawa couplings of the Higgs bosons  $h_i$  in the C2HDM, divided by the corresponding SM Higgs couplings. The expressions correspond to  $[c^e(h_i f f) + ic^o(h_i f f)\gamma_5]$  from Eq. (2.15).

With this choice, the mass of the heaviest neutral scalar is a derived quantity, obeying

$$m_3^2 = \frac{m_1^2 R_{13}(R_{12} \tan \beta - R_{11}) + m_2^2 R_{23}(R_{22} \tan \beta - R_{21})}{R_{33}(R_{31} - R_{32} \tan \beta)}. \quad (2.14)$$

Here,  $m_3^2$  has to be a positive quantity, which is implemented in the optimization algorithm as a constraint that must be satisfied before the fitting procedure is initiated [58, 75, 76].

The imposed  $\mathbb{Z}_2$  symmetry is motivated by the possibility of forbidding tree-level flavour-changing neutral couplings known to be very constrained experimentally. The adopted natural flavour conservation mechanism [4, 5] extends the symmetry to the Higgs-fermion Yukawa sector such that each of the three families of fermions couples to one and only one scalar field. Introducing the up-, down- and lepton-type fermion doublets as  $\Phi_u$ ,  $\Phi_d$  and  $\Phi_\ell$ , for the doublet  $\Phi_i$  ( $i = 1, 2$ ) that respectively couples to up-type, down-type and charged leptons, there are four possible Yukawa types of the softly-broken  $\mathbb{Z}_2$  symmetric 2HDM:

- Type-I:  $\Phi_u = \Phi_d = \Phi_\ell \equiv \Phi_2$
- Type-II:  $\Phi_u \equiv \Phi_2 \neq \Phi_d = \Phi_\ell \equiv \Phi_1$
- Lepton-Specific (LS)  $\Phi_u = \Phi_d \equiv \Phi_2 \neq \Phi_\ell \equiv \Phi_1$
- Flipped  $\Phi_u = \Phi_\ell \equiv \Phi_2 \neq \Phi_d \equiv \Phi_1$ .

The Yukawa Lagrangian for the neutral scalars can be written as

$$\mathcal{L}_Y = - \sum_{i=1}^3 \frac{m_f}{v} \bar{\psi}_f [c^e(h_i f f) + ic^o(h_i f f)\gamma_5] \psi_f h_i, \quad (2.15)$$

where  $\psi_f$  denote the fermion fields with mass  $m_f$ . The coefficients of the CP-even and of the CP-odd part of the Yukawa coupling,  $c^e(h_i f f)$  and  $c^o(h_i f f)$ , are presented in Tab. 2 and will be abbreviated by  $c_f^e$  and  $c_f^o$ , respectively, for the state identified as the 125 GeV scalar. The different families of fermions are identified by choosing  $f$  with the labels  $t$ ,  $b$  and  $\tau$  for up-type, down-type and leptons, respectively.

The aim of our simulations is to study the CP nature of the 125 GeV scalar, identified out of the three  $h_i$  as  $h_{125}$ , with a focus on the possibility of large pseudoscalar  $c_f^o$  couplings.

There are experimental bounds on the CP-odd ( $c_t^o$ ) versus CP-even ( $c_t^e$ ) couplings to the top quark [77]:

$$|\theta_t| = |\arctan(c_t^o/c_t^e)| < 43^\circ \text{ at } 95\% \text{ CL.} \quad (2.16)$$

In more recent LHC data analyses, bounds were also placed on the CP-odd ( $c_\tau^o$ ) versus CP-even ( $c_\tau^e$ ) couplings to the tau lepton [54, 78]:

$$|\theta_\tau| = |\arctan(c_\tau^o/c_\tau^e)| < 34^\circ \text{ at } 95\% \text{ CL.} \quad (2.17)$$

There are no direct bounds on the CP-odd coupling to the bottom quark ( $c_b^o$ ). Reference [29] found the situation summarized in Tab. 1.

The Higgs couplings to the massive gauge bosons  $V = W, Z$  are given by

$$i g_{\mu\nu} c(h_i VV) g_{h^{\text{SM}} VV}, \quad (2.18)$$

with the SM coupling  $g_{h^{\text{SM}} VV}$  given by  $g M_W$  for the  $V = W$  case and  $g M_Z / \cos \theta_W$  for  $V = Z$ , where  $h^{\text{SM}}$  denotes the SM Higgs. Since the signs of  $c_f^e$  and  $c_f^o$  have no absolute meaning and are relative to the sign of  $k_V \equiv c(h_{125} VV)$ , our results are shown with combinations of  $\text{sign}(k_V)c_f^o$  vs.  $\text{sign}(k_V)c_f^e$ .

### 3 The electron EDM

We now turn to a discussion of the eEDM (the contributions from the muon EDM and from non-leptonic EDMs are currently less stringent and thus not considered [25]). For the theoretical predictions, we use the formulae in Refs. [12, 22, 36, 43, 47, 79]. We stress that the calculation as presented in Refs. [36, 47] includes the complete set of non-vanishing contributions to the eEDM in the C2HDM. Although this complete set corresponds to a gauge-independent result, the individual contributions depend in general on the gauge. In this work, after explicitly checking that their sum is gauge independent, we choose the Feynman gauge for these individual contributions. We investigate for the first time the role of the kite diagrams [36] in simulations of the parameter space of the C2HDM satisfying all theoretical and most recent experimental constraints. As discussed above, we also assess the impact of Barr-Zee diagrams with the charm quark (hereafter referred to as charm diagrams). Finally, we comment on diagrams that yield even smaller contributions.

Beyond the question of which diagrams are included, the two-loop eEDM calculation also involves the choice of the renormalization scheme. In particular, different approaches can be adopted for the renormalization prescriptions of the fermion masses. The most common choices are  $\overline{\text{MS}}$  running masses at the scale  $M_Z$  ( $\overline{m}_t(M_Z), \overline{m}_b(M_Z)$ ) [22, 36, 80], or pole mass for the top quark in combination with the running bottom-quark mass at the scale  $\overline{m}_b$  ( $m_t, \overline{m}_b(\overline{m}_b)$ ) [25, 31, 38, 81].<sup>1</sup> For brevity, in what follows we refer to the first choice as the “ $M_Z$ -masses” scheme and to the second as the “pole-masses” scheme. In Ref. [29] it was shown that in the Type-II model with the choice  $h_2 = h_{125}$ , the choice of the renormalisation scheme adopted for the fermion masses in the eEDM calculation is

<sup>1</sup>For the tau lepton, we always use the pole mass,  $m_\tau$ . The same choice was made in Ref. [29]; however, that reference contains a typo, as it states that two mass schemes were considered for that particle.

relevant. Using the  $M_Z$ -masses scheme, it was found that sizable CP-odd components in the  $h_{125}b\bar{b}$  coupling were incompatible with the combined experimental constraints from the upper limit on the eEDM and from cross-section limits from BSM scalar searches. For the pole-masses scheme, by contrast, there remained the possibility of considerable large pseudoscalar components of the Higgs-fermion couplings. In Section 5, we will review this discussion in light of the updated eEDM calculation with kite contributions.

## 4 Sampling

### 4.1 Theoretical and experimental constraints

With the aim of probing the CP nature of the 125 GeV scalar, we perform an extensive scan of the parameter space subject to both theoretical and experimental constraints. In addition to the eEDM calculation described in the previous section, the imposed theoretical requirements include boundedness from below of the scalar potential [82–84], the enforcement of a global electroweak minimum through the discriminant condition that avoids metastable vacua [85], and perturbative unitarity [86–88]. The effects of new physics on electroweak precision observables are evaluated through the oblique parameters  $S$ ,  $T$  and  $U$  [89, 90], which are required to agree at the  $2\sigma$  level with the global electroweak fit of Ref. [91].

Constraints from Higgs precision measurements are imposed by requiring agreement with the LHC determinations of coupling modifiers [92] at  $3\sigma$  and signal strengths [93] at  $2\sigma$ , consistent with CMS data [94], for each individual initial-state  $\times$  final-state production channel. Direct searches for additional scalar states are taken into account by implementing the C2HDM in the software framework `HiggsTools` (HT), version 1.1.3 [95], and running the most recent module `HiggsBounds` (HB), version 1.7. Flavor constraints are incorporated through an explicit calculation of the  $b \rightarrow s\gamma$  process following Ref. [96], requiring agreement with the experimental measurement [97] at the  $3\sigma$  level. As shown in Ref. [98–102], this observable implies the lower bound  $m_{H^\pm} > 580$  GeV at 95% CL ( $2\sigma$ ) in the Type-II C2HDM. The global fit of Ref. [103] confirms this lower bound, and shows that it also holds for the Flipped model.

Constraints from direct LHC searches for CP violation of the Higgs boson are applied after those from Higgs precision measurements discussed above. Specifically, for the CP-violating couplings of  $h_{125}$  to the top quark, we impose the bounds given in Eq. (2.16) [77]. As for the bounds on the CP-violating couplings of  $h_{125}$  to the tau lepton (for short, bounds on  $\theta_\tau$ ), we investigate two alternative approaches: either including the likelihood estimate given by the module `HiggsSignals` (HS) within HT [95], or considering Eq. (2.17) [54, 78]. Concerning the former, a comment is in order. When sampling the parameter space subject to all the constraints described above (with the bounds on  $\theta_\tau$  implemented via the public version of the HS module), we rapidly encounter a regime in which all points exhibiting sizable pseudoscalar Higgs–fermion couplings are excluded by HS. In App. A, we explain in detail the origin of this tension, and how we modified the dataset used by HS to address this issue. In what follows, whenever we consider the HS to impose bounds on  $\theta_\tau$ , we always use the modified dataset. A more detailed discussion is provided in App. A.



## 4.2 Sampling techniques

In our results, we shall be mainly interested in the Type-II and Flipped models. For a generic assignment of  $h_i$  to  $h_{125}$ , the sampling regions can be presented in a compact way for both models.

$$\begin{aligned}
G_F &= 1.16638 \times 10^{-5} \text{ GeV}^{-2} & M_Z &= 91.1876 \text{ GeV} \\
\alpha_{\text{em}}^{-1}(M_Z) &= 127.92 & M_W &= 80.385 \text{ GeV} \\
\alpha_{\text{em}}^{-1} &= 137.035999 & m_\tau &= 1.77682 \text{ GeV} \\
m_t &= 172.5 \text{ GeV} & \bar{m}_t(M_Z) &= 163 \text{ GeV} \\
\bar{m}_b(\bar{m}_b) &= 4.7800 \text{ GeV} & \bar{m}_b(M_Z) &= 2.88 \text{ GeV} \\
\Gamma_W &= 2.08430 \text{ GeV} & \Gamma_Z &= 2.49427 \text{ GeV}
\end{aligned} \tag{4.1}$$

After setting  $m_{125} = 125.09 \text{ GeV}$ , we can write the sampling of the independent parameters as

$$\begin{aligned}
m_{1 < h_{125}} &\in [15.0, 122.5] \text{ GeV}; & m_{2 > h_{125}} &\in [127.5, 1000] \text{ GeV}; & m_{H^\pm} &\in [580, 1000] \text{ GeV}; \\
\tan \beta &\in [0.3, 30.0]; & \text{Re}(m_{12}^2) &\in [\pm 10^{-1}, \pm 10^7]; & \alpha_1, \alpha_2, \alpha_3 &\in \left[-\frac{\pi}{2}, \frac{\pi}{2}\right].
\end{aligned} \tag{4.2}$$

However, a purely random sampling of the parameter space is highly inefficient in identifying configurations with large pseudoscalar fermion-Higgs couplings. As discussed above, the mass parameter  $m_3^2$  is a derived quantity and it can become negative in parts of the sampled space. These points must be discarded as they are unphysical. In addition, for the choice  $h_2 \equiv h_{125}$  the heavy neutral scalar is further required to be approximately degenerate in mass with the charged Higgs in order to comply with experimental constraints [104]. Still, obtaining an experimentally viable solution in the resulting reduced parameter region is a slow process.

We therefore adopt two complementary strategies, which we label Strategy 1 and Strategy 2 in the following. In the first, we perform a guided scan in which the parameter space is explored close to the phenomenological boundary, iteratively increasing the pseudoscalar component of the Higgs-fermion couplings [25, 29, 57]. In the second, we employ an AI-based black-box optimisation technique, originally introduced in Ref. [69], subsequently applied to a real 3HDM in Ref. [70], and later extended to 3HDMs with explicit CP violation in the scalar sector [58, 76].

In Strategy 1, the sampling is initiated from points for which the squared mass of the third neutral scalar is already physical. In contrast, the ML method of Strategy 2 — which does not rely on pre-existing training data — implements a hierarchical optimization procedure in which the positivity of the squared mass is enforced as a hard constraint within the loss function. Only after this requirement is satisfied does the algorithm proceed to optimize the remaining theoretical and experimental constraints [58, 75, 76].

The sampling algorithm employed in Strategy 2 is the Covariant Matrix Adaptation Evolutionary Strategy (CMA-ES) [105, 106]. By construction, individual CMA-ES runs

are statistically independent: each run is initialized with a new choice of the mean vector and covariance matrix, and the optimization proceeds using only the information generated within that run. While this fully blind initialization ensures independence, it was found to lead to an uneven coverage of the parameter space, with distinct regions being explored in isolation and the overall sampling density remaining sparse in intermediate domains. To mitigate this limitation and improve the continuity and efficiency of the exploration, CMA-ES also allows for initialization using the mean vector and covariance matrix obtained from previous optimization runs, hereafter referred to as *seeded runs*. When combined with an integrated anomaly-detection-based novelty reward mechanism, implemented via a Histogram-Based Outlier Score (HBOS) [107] evaluated on a selected subset of parameters or observables of interest, this strategy yields a more uniform and coherent exploration of the model’s parameter space and its associated physical implications.

We conclude this section with two final remarks. First, all datasets used to produce the plots in this paper — under both Strategy 1 and Strategy 2 — are generated by imposing all constraints described in Sec. 4.1, with the exception of those associated with  $\theta_\tau$ . As discussed at the end of Sec. 4.1, two alternative implementations of the  $\theta_\tau$  constraints are considered; hence, whenever these constraints are imposed, we explicitly state which alternative is adopted. Second, all plots presented in this work that rely on Strategy 2 are based on samples containing at least  $\mathcal{O}(10^7)$  points.

## 5 Results for Type-II with $h_2 = h_{125}$

Motivated by the discussion above on the choice of the fermion-mass renormalization schemes in the eEDM calculation, we focus in this section on the Type-II model with  $h_2 \equiv h_{125}$ . Besides the usual Barr-Zee diagrams [43–46] (whose diagrams with fermion loops include only third generation fermions), we start by including only the kite diagrams in our eEDM calculation. This study is carried out in Secs. 5.1 and 5.2, which implement Strategy 1 and Strategy 2, respectively. At the end of Sec. 5.2, we discuss the role of the contributions of other diagrams to the eEDM. In Sec. 5.3, we then turn to a specific region of the parameter space characterized by small values of the scalar mass  $m_1$ . Finally, Sec. 5.4 is devoted to a detailed investigation of the role played by the charm diagrams in the eEDM calculation.

### 5.1 Phenomenology with Strategy 1

Figure 1 shows two plots of the plane  $\text{sign}(k_V)c_b^o$  vs.  $\text{sign}(k_V)c_b^e$  generated with Strategy 1, imposing the current eEDM limit (left) and imposing a projected eEDM limit  $1.0 \times 10^{-33} \text{ e} \cdot \text{cm}$  [51–53] (right). In the calculation of the eEDM in both panels, the  $M_Z$  masses are used and, as discussed above, only the usual Barr-Zee diagrams and the kite diagrams are included. The red points correspond to parameter points that fulfill all constraints discussed in section 4 except those on  $\theta_\tau$ , while the purple points additionally impose those constraints using HS. The figure shows that, for both eEDM scenarios considered in the panels, the dominant limitation on the magnitude of the pseudoscalar component of  $h_{125}$  arises from the bounds on  $\theta_\tau$ . The figure also shows that the valid (purple) points

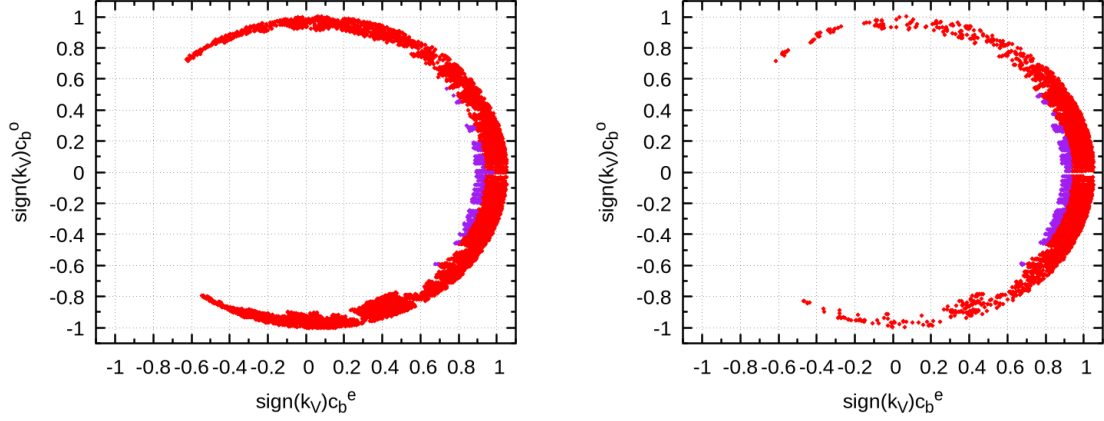


**Figure 1:** Points on the plane  $\text{sign}(k_V)c_b^o$  vs.  $\text{sign}(k_V)c_b^e$  obtained with Strategy 1 in the Type-II C2HDM with  $h_{125} = h_2$ . The purple points include all constraints, including those relative to  $\theta_\tau$  implemented via HS, while the red points include all constraints except those relative to  $\theta_\tau$ . Left panel: current eEDM limit  $4.1 \times 10^{-30} \text{ e} \cdot \text{cm}$ . Right panel: projected eEDM limit  $1.0 \times 10^{-33} \text{ e} \cdot \text{cm}$ . See text for details.

are all close to the SM solution  $(\text{sign}(k_V)c_b^e, \text{sign}(k_V)c_b^o) = (1, 0)$ ; in particular, no points can be found close to the so-called “wrong-sign” solution  $(\text{sign}(k_V)c_b^e, \text{sign}(k_V)c_b^o) = (-1, 0)$ . Finally, we confirm that the points sampled are in agreement with the public code ScannerS [108], now also updated to include the kite diagrams in the eEDM calculation.

In Fig. 2, we assess the impact of the kite diagrams on the eEDM prediction. The blue points show the total predicted value of the eEDM, the red ones correspond to the same prediction with the kite-diagram effects subtracted, and the green points represent the class of diagrams yielding the largest contribution to the eEDM for each sampled parameter point. From this comparison, we confirm the result of Ref. [36] that the inclusion of the kite diagrams induces  $\mathcal{O}(1)$  corrections to the eEDM prediction for the dataset sampled.

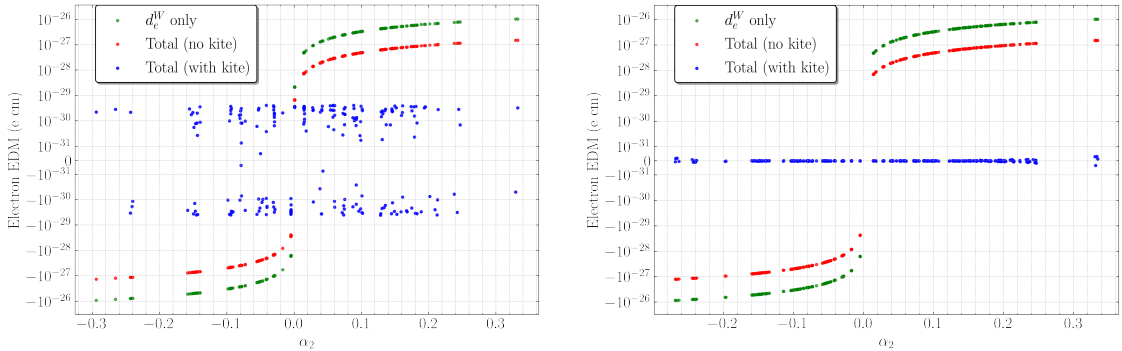


**Figure 2:** Different contributions to the eEDM for the set of points sampled: total contribution (blue), total contribution except for the kite diagrams (red), contribution of the dominant class of diagrams (green). Left panel: current eEDM limit  $4.1 \times 10^{-30} \text{ e} \cdot \text{cm}$ . Right panel: projected eEDM limit  $1.0 \times 10^{-33} \text{ e} \cdot \text{cm}$ .

## 5.2 Phenomenology with Strategy 2

As mentioned in the Introduction, standard scans can completely miss certain valid regions of the parameter space — regions where new phenomenology may be possible. Having discussed in the previous section the values found on the plane  $\text{sign}(k_V)c_b^o$  vs.  $\text{sign}(k_V)c_b^e$  with the standard scans of Strategy 1, we now turn to ML techniques. The datasets considered below include optimization runs seeded with a subset of points obtained from earlier unseeded runs. The simulations are designed to determine the maximal allowed size of the CP-odd fermionic coupling, imposing the bounds on  $\theta_\tau$  either through HS or through Eq. (2.17). All optimization runs incorporate a novelty-reward mechanism targeting large CP-odd fermion couplings.

The results are shown in Fig. 3. As before, the calculation of the eEDM is performed including the usual Barr-Zee diagrams and the kite diagrams. We now differentiate the eEDM calculation performed with the  $M_Z$ -masses scheme (left panel) from the calculation performed with the pole-masses scheme (right panel).<sup>2</sup> Points shown in red satisfy all constraints described in Sec. 4, with the exception of those on  $\theta_\tau$ . The remaining points

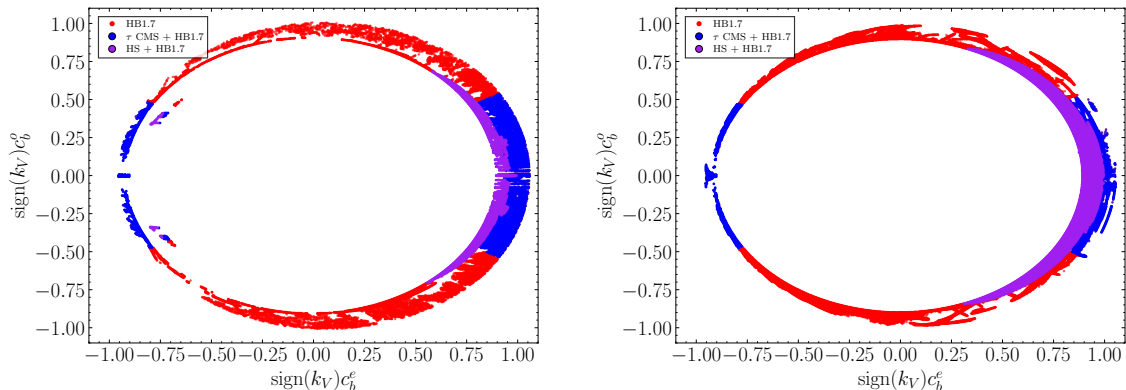


**Figure 3:** Points on the plane  $\text{sign}(k_V)c_b^o$  vs.  $\text{sign}(k_V)c_b^e$  obtained with Strategy 2 in the Type-II C2HDM with  $h_{125} = h_2$ . Red points pass all constraints except those on  $\theta_\tau$ ; the remaining points additionally impose the latter constraint: either via HS (in purple) or via Eq. (2.17) (in blue). Left: eEDM calculated in the  $M_Z$ -masses scheme. Right: eEDM calculated in the pole-masses scheme.

additionally impose the latter bounds: either via HS (in purple) or via Eq. (2.17) (in blue). This figure should be directly compared with Fig. 1. Several noteworthy features emerge from this comparison.

First, Fig. 3 clearly demonstrates the substantial advantage of the ML-based search over the standard scanning strategy of Fig. 1. The ML approach uncovers a significantly larger region of parameter space with large CP-odd couplings. In particular, it reveals a viable region in the vicinity of the wrong-sign solution — which, as noted above, is entirely absent in the standard scan.

Second, the qualitative features of the ML results are similar for both  $M_Z$ -masses and pole-masses schemes. Dedicated tests show that this similarity disappears once the

<sup>2</sup>For the definition of the  $M_Z$ -masses and the pole-masses scheme, cf. Sec. 3.

kite diagrams are excluded, in agreement with the findings of Ref. [29] (see, in particular, the comparison between the right panel of Fig. 1 and the left panel of Fig. 2 therein). This provides further confirmation of the central role of the kite diagrams, as previously emphasized in Ref. [36]. Their importance is not unexpected, given that, as discussed before, these diagrams are required to ensure gauge invariance of the eEDM calculation [36]. As a consequence, non-negligible values of  $|c_b^o|$  in the Type-II C2HDM with  $h_{125} \equiv h_2$  are found to be phenomenologically viable, constrained primarily by the measurements of  $\theta_\tau$ .

Third, Fig. 3 illustrates the impact of the two different implementations of the  $\theta_\tau$  constraint. The blue points cover the same width of the ellipse as the red points, but they stop abruptly for  $|\theta_\tau| \geq 34^\circ$  due to the constraint of Eq. (2.17). The region covered by the purple points, by contrast, has a narrower width than the red points, and they are not constrained by the abrupt cut at  $|\theta_\tau| = 34^\circ$ . Both these features result from the likelihood estimate given by HS.

Finally, in the  $M_Z$ -masses scheme shown in the left panel of Fig. 3, we observe isolated regions near  $|c_b^o| \sim 0.4$  and  $\text{sign}(k_V)c_b^e \sim -0.75$  that are absent in the pole-masses scheme displayed in the right panel. These points correspond to comparatively light scalar masses,  $m_1 \sim 50$  GeV. We return to a detailed discussion of this region in Sec. 5.3 below.

An interesting question concerns the possibility of accommodating increasingly stringent eEDM bounds while still obtaining parameter points with the largest  $|c_b^o|$  components compatible with current experimental constraints. This issue is illustrated in Fig. 4.<sup>3</sup> The plot shows that, irrespective of how stringent the eEDM bound becomes — even down

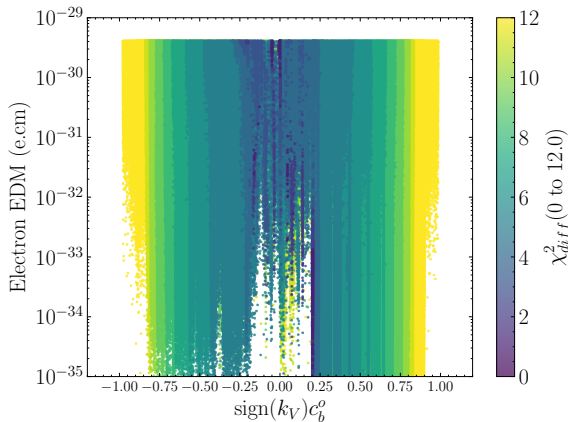


**Figure 4:** Points obtained with Strategy 2 in the Type-II C2HDM with  $h_{125} = h_2$ , on the plane eEDM prediction (calculated with the pole-masses scheme) vs.  $\text{sign}(k_V)c_b^o$ . The color code shows the lowest possible  $\chi^2$  calculated with HS.

<sup>3</sup>As before, the calculation of the eEDM is performed including the usual Barr-Zee diagrams and the kite diagrams, assuming the pole-masses scheme. Furthermore, and as usual, the plot is generated from datasets satisfying all constraints described in Sec. 4.1 except those on  $\theta_\tau$ . On the other hand, the figure does not commit to a specific prescription for imposing the  $\theta_\tau$  constraints. If one adopts the alternative based on Eq. (2.17), only the points lying within the range of  $\text{sign}(k_V)c_b^o$  spanned by the blue points in the right panel of Fig. 3 are considered valid. If, instead, the HS alternative is followed, the color coding of the figure, representing the  $\chi^2_{\text{diff}}$  obtained from HS, allows the  $\theta_\tau$  constraint to be imposed at the desired confidence level within that framework.

to  $10^{-35}$  e·cm — it is always possible to identify regions of parameter space that allow for sizable  $|c_b^o|$  components, provided the parameters are tuned so that large cancellations conspire to satisfy progressively stronger eEDM constraints.

Although not shown explicitly, we also performed dedicated runs that led to further observations. First, percent-level variations in the input mass values still permit the identification of parameter sets for which the required cancellations to satisfy the eEDM bounds occur. It is found, however, that such small changes require significant changes in the remaining input parameters in order to still fulfill the required cancellations. This behavior is not unexpected, given that the cancellations involve contributions from very different diagrams. Second, once the eEDM sensitivity reaches the level of  $10^{-33}$  e·cm, the contributions of several types of diagrams not included so far in our eEDM calculation (such as Barr-Zee diagrams with quarks beyond the third generation, as well as one-loop diagrams) become numerically relevant.

### 5.3 Isolated regions with small $h_1$ masses

As discussed above, the isolated regions located around  $|c_b^o| \sim 0.4$  and  $\text{sign}(k_V)c_b^e \sim -0.75$  in the plot with the  $M_Z$ -masses scheme of Fig. 3 (left panel) correspond to scenarios with small scalar masses,  $m_1 \sim 50$  GeV. We probe this feature in more detail in Fig. 5, which displays the subset of points from the left panel of Fig. 3 with  $m_1 < 60$  GeV. The figure

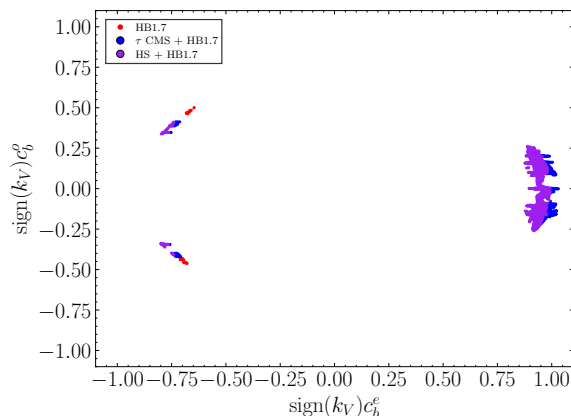


**Figure 5:** The same as the left panel of Fig. 3, but considering exclusively points with  $m_1 \leq 60$  GeV.

reveals a region close to the SM-like point  $(\text{sign}(k_V)c_b^e, \text{sign}(k_V)c_b^o) = (1, 0)$ , as well as an isolated region near  $|c_b^o| \sim 0.4$  and  $\text{sign}(k_V)c_b^e \sim -0.75$ . This latter region is disconnected from the vicinity of the wrong-sign solution  $(\text{sign}(k_V)c_b^e, \text{sign}(k_V)c_b^o) = (-1, 0)$ , for which no parameter points with small  $m_1$  masses survive. In fact, the isolated region corresponds to a very narrow mass window,  $51 \text{ GeV} \lesssim m_1 \lesssim 53 \text{ GeV}$ .

We note that the analogous plot obtained using the pole-masses scheme does not exhibit these isolated regions. This behavior is easy to understand. As discussed above, the parameter regions compatible with the eEDM constraints arise from very precise cancellations among different diagrammatic contributions, typically at the per-mil level. Thus, small variations in the input mass parameters lead to large shifts in the remaining param-

eter space, making it unsurprising that a narrow region present for the  $M_Z$ -masses scheme disappears for the pole-masses scheme.

To investigate the range of values taken by  $m_1$ , Fig. 6 displays all points shown in Fig. 3, now projected onto the plane  $\text{sign}(k_V)c_b^o$  versus  $m_1$ . Intermediate values of  $m_1$  are excluded by HB through direct searches for additional Higgs bosons, as reported in Refs. [109–111]. From the left panel, one observes side bands with  $|c_b^o| > 0.3$  clustered around  $m_1 \sim 50$  GeV,

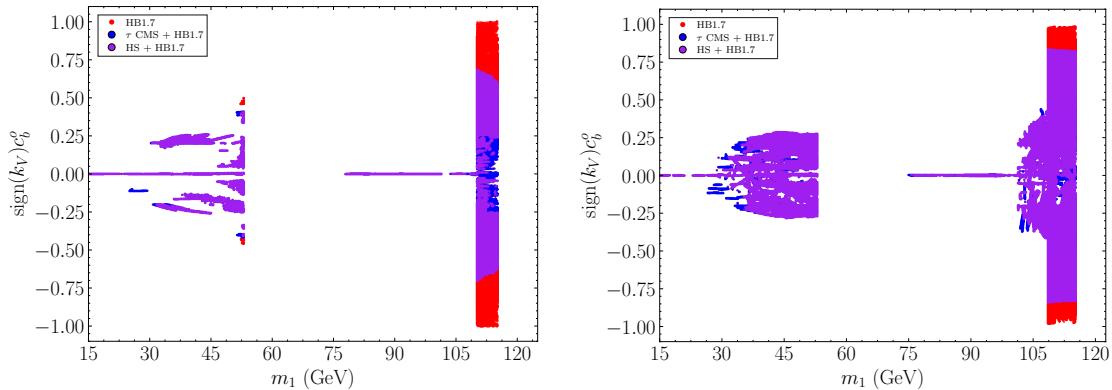


**Figure 6:** The same as in Fig. 3, but for the plane  $\text{sign}(k_V)c_b^o$  vs.  $m_1$ .

corresponding to the isolated regions previously identified in Figs. 3 (left) and 5. These regions lie close to the current exclusion boundary. Given the strong sensitivity of these features to the precise input parameters, we do not attribute particular physical significance to the isolated regions appearing when the fermion masses are defined in the  $M_Z$ -masses scheme.

#### 5.4 The charm diagrams

Up to now, we included in our calculations for the eEDM the new kite diagrams from Ref. [36], besides the usual Barr-Zee diagrams (which, we recall, contain only fermions of the third generation). One could wonder whether a Barr-Zee diagram with an intermediate charm quark would be important given the current experimental bounds. As we will now show, this is indeed the case, despite their mass suppression.

We have taken some of the points in the left panel of Fig. 3, which obey the current eEDM bounds and which were calculated *without* taking into consideration the charm diagrams; we then calculated, for those points, what the contribution of the charm diagrams would be. For the charm quark, we chose the running  $\overline{\text{MS}}$  mass  $\overline{m}_c$  at the scale  $\overline{m}_c$ , namely  $\overline{m}_c(\overline{m}_c) = 1.2$  GeV [112]. The result is shown in Fig. 7, which displays separately the contributions from the dominant class of diagrams (green), the kite diagrams (pink) and the charm diagrams (red). As was already discussed in the context of Fig. 2, it is clear that the kite diagrams are crucial for the cancellation. The plot also shows that the charm contribution comes in at the order of a few times  $10^{-29}$  e.cm, well above the current experimental level of  $4.1 \times 10^{-30}$  e.cm [50]. Thus, it spoils the cancellation, and the points become disallowed.

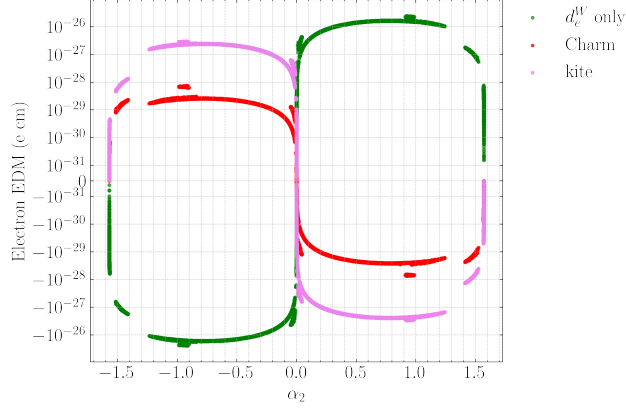


**Figure 7:** Points of the left panel of Fig. 3, now projected on the plane eEDM vs.  $\alpha_2$ . Besides the contributions from the kite diagrams (pink) and the dominant diagrams (green), both of which were included in the calculation of the eEDM in Fig. 3, the plot also shows the contribution of the charm diagrams (red).

Of course, although the charm contributions spoil the cancellation of points obtained without it, new points can be found which, when including the charm contribution, produce new precise cancellations, in line with the experimental bound. Thus, we have performed a new simulation including both kite and charm contributions, shown in Fig. 8. In the left panel, we show the results in the above defined  $M_Z$ -masses scheme and with the charm-quark mass chosen as  $\overline{m}_c(\overline{m}_c) = 1.2$  GeV. The right panel displays results obtained in the pole-masses scheme with the on-shell charm quark mass chosen as  $m_c = 1.51$  GeV [113]. Comparing this figure (which includes the charm diagrams) with Fig. 3 (which does not), we see that all the features discussed previously remain. In conclusion, including the charm contributions alters the set of valid points obtained, but it does not preclude compliance with the current eEDM experimental bounds, nor does it alter the qualitative  $c_b^o$  features.

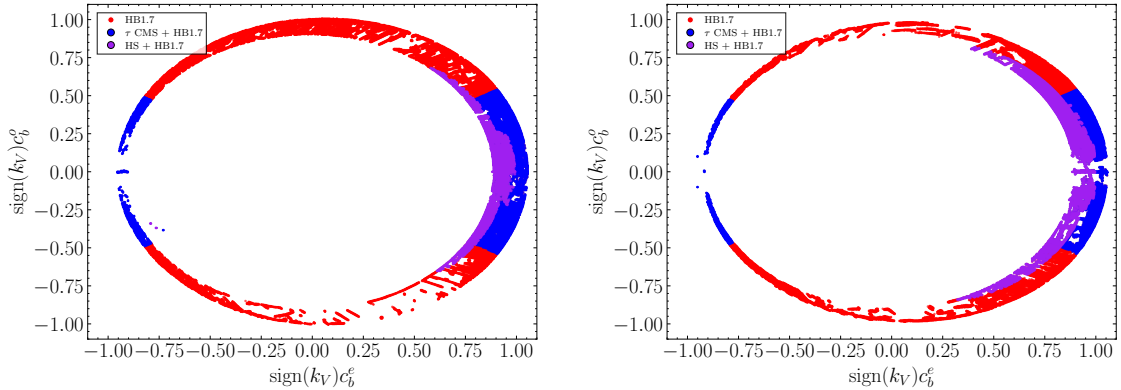


**Figure 8:** Same as in Fig. 3, but for points which include the charm diagrams in the eEDM prediction.



## 6 Revisiting other cases of the C2HDM

Having established the importance of both kite and charm contributions to the eEDM, we revisit all scenarios listed in Table 1 using ML techniques (Strategy 2). In the Type-I model, the CP-odd couplings of all fermions are universal and are therefore strongly constrained by the top-quark sector, forcing them to remain very close to their SM values for all choices of mass ordering. We further verify that no viable solutions with large  $|c_b^o|$  components exist in the Type-II and Flipped models with  $h_3 = h_{125}$ , in agreement with the conclusions of Ref. [25].

We also find no viable points with large  $|c_b^o|$  for the mass choice  $h_1 = h_{125}$ . This is shown for Type-II and Flipped in Fig. 9, and the limitation is due to a combination of searches for heavy resonances [114–116], which is checked by HT. Nevertheless, the recent Ref. [117] makes the point that there may be some large CP-violating signals in Type-II with  $h_1 = h_{125}$ .

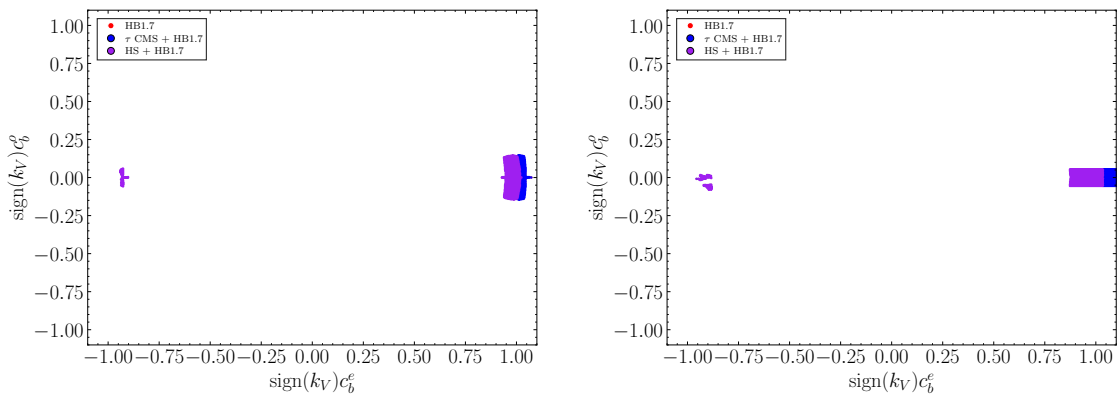


**Figure 9:** Points on the plane  $\text{sign}(k_V)c_b^o$  vs.  $\text{sign}(k_V)c_b^e$  obtained with Strategy 2, in Type-II with  $h_{125} = h_1$  (left) and Flipped with  $h_{125} = h_1$  (right). In both panels, the eEDM is calculated with the pole-masses scheme. The color code is as in Fig. 3.

A few remarks are in order. First, looking at Fig. 13 in Ref. [117], we agree that indeed there are no large  $|c_b^o|$  couplings (for  $h_{125}$ ). Second, even when  $s_2 = 0$  (implying that  $h_1$  is a pure scalar), Ref. [11] points out in their endnote 20 that there will still be CP violation in the heavier scalars, proportional to  $J_1 \propto (m_1^2 - m_2^2)(m_1^2 - m_3^2)(m_2^2 - m_3^2) \cos(\beta - \alpha_1) \sin^2(\beta - \alpha_1) \cos(\alpha_3) \sin(\alpha_3)$ . This source of CP violation only vanishes if the sine or cosine of  $\beta - \alpha_1$  or of  $\alpha_3$  vanish, or if the heavier two states are degenerate. That is, it vanishes in the exact alignment limit, where  $h_1$  coincides exactly with the SM predictions, as re-emphasized in Ref. [14]. What Ref. [117] brings to the table is that, as one goes slightly away from the exact alignment limit, significant CP-violating signals are possible in some observables, other than  $c_b^o$ .

We now turn to the Flipped model, with  $h_2 = h_{125}$ . Our results are presented in Fig. 10. This case does allow for maximal  $|c_b^o|$  couplings consistent with all current experimental data. What this means is that, in this case, one can have  $h_{125}$  coupling mostly as a scalar to the top quark, while it couples as a pure pseudoscalar to the bottom quark. Again, we

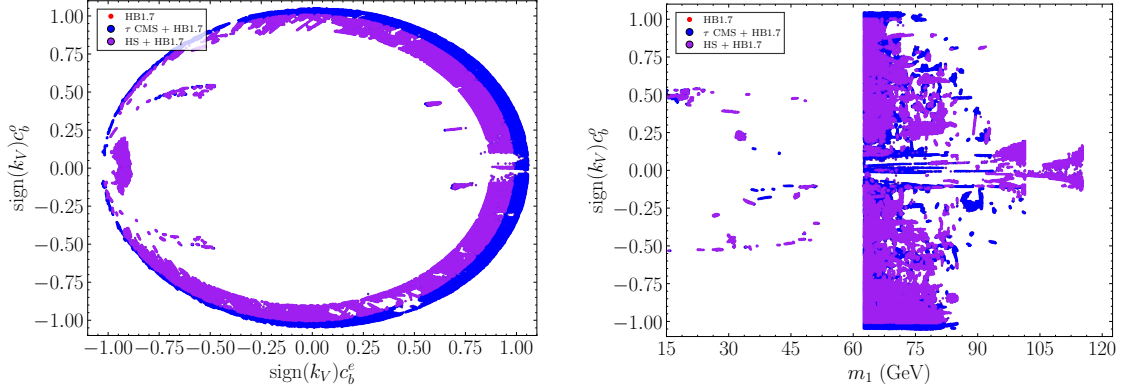


**Figure 10:** Flipped C2HDM with  $h_2 = h_{125}$ , with the eEDM calculated with the  $M_Z$ -masses scheme, including both kite and charm contributions. The color code is as in Fig. 3. Left: plane  $\text{sign}(k_V)c_b^o$  vs.  $\text{sign}(k_V)c_b^e$ . Right: plane  $\text{sign}(k_V)c_b^o$  vs.  $m_1$ .

notice the presence of the isolated regions (with lower radius) with  $m_1 \leq 60$  GeV. For this case, the points have dominant diagrams of order  $10^{-29}$  e.cm, unlike the order  $10^{-27}$  e.cm individual contributions occurring in the case Type-II with  $h_2 = h_{125}$ .

## 7 Conclusions

We have carried out a comprehensive exploration of the parameter space of the C2HDM using recent ML techniques designed to efficiently probe complex, high-dimensional BSM scenarios, even in the absence of pre-existing training data. To this end, we employed an Evolutionary Strategy algorithm [69] to identify phenomenologically viable points, combined with an anomaly-detection-based Novelty Reward mechanism [70]. This framework enables a robust and reliable exploration of the model’s parameter space and, consequently, of its potentially observable physical predictions.

We have concentrated on regions of the parameter space allowing for large components of  $c^o$ , the pseudoscalar coupling between the 125 GeV Higgs boson ( $h_{125}$ ) and fermions. In particular, we were interested in the striking possibility, first pointed out in Ref. [21], that  $h_{125}$  couples to the top quark as a pure scalar, while it couples to the bottom quark as a pure pseudoscalar. Models with CP violation in the scalar sector usually must contend with large contributions to the eEDM, which is very constrained by current experiments to lie below  $4.1 \times 10^{-30}$  e.cm [50]. Recent articles [36, 47] have pointed out the importance of kite diagrams to the theoretical issue of gauge independence of the final result, and to the practical issue of taking into account all numerically relevant contributions. Re-analyzing the C2HDM with the aid of ML, we confirmed that kite diagrams are paramount, and we further demonstrated that, at the current level of experimental precision, charm-quark Barr-Zee contributions must also be taken into account.

In the process, we investigated the sensitivity of the eEDM calculation to the renormalization prescriptions for the fermions masses, by comparing  $\overline{\text{MS}}$  running masses at the scale  $M_Z$  with pole masses. We found that, using the kite diagrams, the qualitative predic-

tions for  $c^o$  made with either choice remain the same (although for different points in the model's parameter space). Moreover, the cancellations required to obey the current eEDM bound are still possible if the bound is improved by three orders of magnitude. As a result, such measurements will not constrain the significant  $c^o$  possibilities still available. We thus strongly encourage a continued effort to improve the direct probes for  $c^o$  at LHC. We should add that, in the C2HDM, it is not possible to accommodate large values for  $c^o$  involving the top quark. But that possibility does exist in the C3HDM, as shown in Refs. [58, 76]. Hence, improved direct measurements of the CP-odd  $h_{125}$  to the top quark are also highly desirable.

Performing a full analyses of all model types and  $h_{125}$  assignments, we reach the conclusions shown in Table 3. In Type-II with  $h_2 = h_{125}$ ,  $c_b^o = c_t^o$  is only limited by LHC's

Type	I	II	LS	Flipped
$h_1 = h_{125}$	×	×	$\tau$	×
$h_2 = h_{125}$	×	<u><math>\tau</math></u>	$\tau$	<u><math>\checkmark</math></u>
$h_3 = h_{125}$	×	×	$\tau$	×

**Table 3:** Updated version of Table 1 after the analysis described in this paper. Underlined entries mark changes w.r.t. Ref. [29].

searches for CP violation in tau decays [54, 78]; the results are shown in Fig. 8. In contrast, in the Flipped model with  $h_2 = h_{125}$ ,  $c_b^o$  can be maximal ( $c_b^e = 0$ ); the results are shown in Fig. 10. In this second case, the wrong-sign solution ( $c_b^e = -1, c_b^o = 0$ ) is also still viable.

In summary, we have performed a full analysis of the C2HDM utilizing ML to access the full parameter space and observable predictions, complying with the full two-loop eEDM calculation. The cases still viable call for increased experimental efforts to probe CP-odd  $h_{125}$  couplings to quarks directly.

## Acknowledgments

We thank Wolfgang Altmannshofer for discussions. D.F. thanks Joachim Brod, Gino Isidori, Kilian Möhling, Ulrich Nierste, Zachary Polonsky and Dominik Stöckinger for discussions, and the Particle Theory Group at the UZH for its hospitality and support. The work of R.B., D.F. and M.M. is supported by the Deutsche Forschungsgemeinschaft (DFG, German Research Foundation) under grant 396021762-TRR 257. K.E. acknowledges financial support from the Avicenna-Studienwerk. The work of J.C.R., J.P.S., M.G. and R.S. is supported in part by the Portuguese Fundação para a Ciência e Tecnologia (FCT) through the PRR (Recovery and Resilience Plan), within the scope of the investment "RE-C06-i06 - Science Plus Capacity Building", measure "RE-C06-i06.m02 - Reinforcement of financing for International Partnerships in Science, Technology and Innovation of the PRR", under the projects with references 2024.01362.CERN and 2024.03328.CERN; the work is also supported by FCT under Contracts UIDB/00777/2020, UIDP/00777/2020 and UID/00618/2025. M.G. is additionally supported by FCT with a PhD Grant (reference 2023.02783.BD). The FCT projects are partially funded through POCTI (FEDER), COMPETE, QREN and the EU.

## A $\chi^2$ exclusion

As explained at the end of Sec. 4.1, using the public version of the HS module to impose bounds on  $\theta_\tau$  leads to a systematic exclusion of parameter points. In this appendix, we provide a detailed illustration of this issue and clarify its origin. For definiteness and ease of presentation, we focus on the representative case of Type-II with  $h_2 = h_{125}$ . We stress, however, that the behavior discussed below is generic and persists in all other realizations of the C2HDM.

The systematic exclusion can be seen by considering the left panel of Fig. 11, which shows points that satisfy all constraints discussed in Sec. 4.1 except those relative to  $\theta_\tau$ . These points correspond exactly to the red points in the left panel of Fig. 1 and amount to

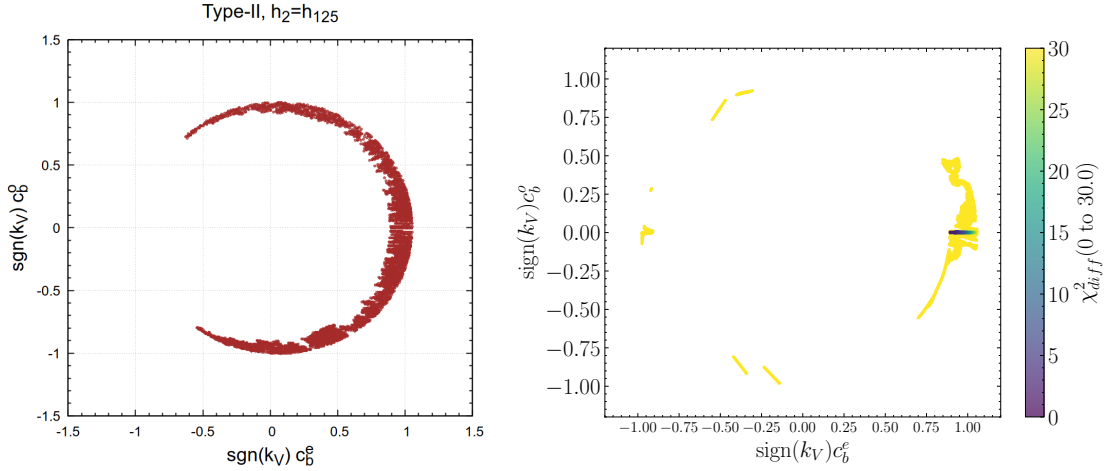


**Figure 11:** Points on the plane  $\text{sgn}(k_V)c_b^o$  vs.  $\text{sgn}(k_V)c_b^e$  in the Type-II C2HDM with  $h_{125} = h_2$  passing all constraints except those relative to  $\theta_\tau$ . Left: points obtained with Strategy 1. Right: points obtained with Strategy 2, with 10000 points per convergence and an unseeded run. On the right, all the (yellow) points that fail HS have  $\chi^2_{\text{diff}}$  of order 150.

a total of 4096 points. The exclusion is verified by realizing that, once the  $\theta_\tau$  constraints are applied via HS, less than 10 points survive. One might suspect that this dramatic reduction arises from limitations of the scanning procedure itself. After all, the left panel of Fig. 11 (like the corresponding panel of Fig. 1) was obtained using Strategy 1, which relies on standard parameter scans. To test this hypothesis, we repeated the analysis using Strategy 2. The result is shown in the right panel of Fig. 11, which displays the resulting values of  $\chi^2_{\text{diff}}$ , which are defined in Sec. 4.1 and computed by HS. This plot demonstrates that the same pattern persists: only a very small number of points yields acceptably low values of  $\chi^2_{\text{diff}}$ . Furthermore, all such points lie very close to the SM limit.

To better understand this issue, we isolate four points from Fig. 11: two from the left panel (Points 1 and 3) and two from the right one (Points 2 and 4). The points are described in detail in Table 4. Points 1 and 2 describe large pseudoscalar couplings, while Points 3 and 4 describe small ones. Only Point 3 passes HS, as it is the only one leading to a value of  $\chi^2$  close to the SM, around 150. The remaining points describe a  $\chi^2$  well above 150.

Parameters	Point 1	Point 2	Point 3	Point 4
$m_1$	111.17800	117.61647	92.42560	109.20862
$m_2$	125.09000	125.00000	125.09000	125.00000
$m_3$	676.09279	676.12103	642.07726	647.28183
$m_{H^\pm}$	675.95296	653.76571	641.68967	652.61301
$\alpha_1$	-0.12294140	-0.09918623	-0.20081799	-0.17832599
$\alpha_2$	0.42298603	-1.00353030	0.00634782	-0.00571511
$\alpha_3$	0.10171668	-0.18011110	0.00285759	-0.00211328
$\beta$	1.45177530	1.45820750	1.35522670	1.39790230
$\text{Re}(m_{12}^2)$	10664.92700	37155.30600	1186.99800	1930.94000
$c_t^o$	-0.011073	0.01088342	-0.00006257	0.00003691
$c_b^o$	-0.77427177	0.85132203	-0.00130500	0.00121010
$c_\tau^o$	-0.77427177	0.85132203	-0.00130500	0.00121010
$\mu_{ggF \times \gamma\gamma}$	0.8653	0.9369	0.9904	0.8637
$\mu_{ggF \times ZZ}$	0.9676	1.0771	1.1037	0.9572
$\mu_{ggF \times WW}$	0.9676	1.0771	1.1037	0.9572
$\mu_{ggF \times \tau\tau}$	1.0371	1.0586	0.9599	1.0177
$\mu_{ggF \times bb}$	1.0378	1.0595	0.9599	1.0177
$\mu_{ggF \times Z\gamma}$	0.9298	1.0295	1.0610	0.9214
$\chi^2$	333.89	351.95	154.55	224.20
$\chi^2$ w/o Ref. [54] as a whole	183.0112	185.3248	153.5897	178.0807
$\chi^2$ w/o $\mu_{ggH \times \tau\tau} = 0.59_{-0.32}^{+0.28}$	186.6076	195.5573	154.1852	178.4548

**Table 4:** Details of four points from Fig. 11. In the public HS implementation, the SM reference value is  $\chi_{\text{SM}}^2 = 152.54$ . Removing the CMS:2021sd result [54] in its entirety reduces this value to  $\chi_{\text{SM}}^2 = 150.2$ , while removing only the  $\mu_{ggH \times \tau\tau}$  sub-measurement from CMS:2021sd [54] yields  $\chi_{\text{SM}}^2 = 150.8875$ .

To investigate the origin of the values of  $\chi^2$ , we examine the individual contributions to  $\chi^2$  of a certain point. This is done using the `chisqContributions(pred)` routine provided by HT, which allows for a comparison of all individual measurements.<sup>4</sup> As stated in the documentation, this procedure neglects correlations and multiplicative factors, implying that the sum of the individual contributions does not coincide with the  $\chi^2$  obtained from the full combined measurement. Yet, this analysis reveals that Ref. [54] (corresponding to measurement number 13 in the HS public code) yields an anomalously large contribution to  $\chi^2$ . This is confirmed by explicitly removing this measurement from the calculation, as shown in the second-to-last line of Table 4.

What exactly is the issue with Ref. [54]? This reference is implemented in HS as a multiplicity of submeasurements. Two of them are  $\mu_{ggH}^{\tau\tau}$  and  $\text{sign}(k_V)c_\tau^o$  vs.  $\text{sign}(k_V)c_\tau^e$ , whose implementation in HS is shown in the left and right panels of Fig. 12, respectively. While the latter yields a physically sensible behavior — crucial for the analysis presented in this work (see the discussion in Sec. 5.2) — the former leads to an unexpected outcome: the SM point

<sup>4</sup>See the HiggsTools documentation: [HiggsSignals \(chisqContributions\)](#)

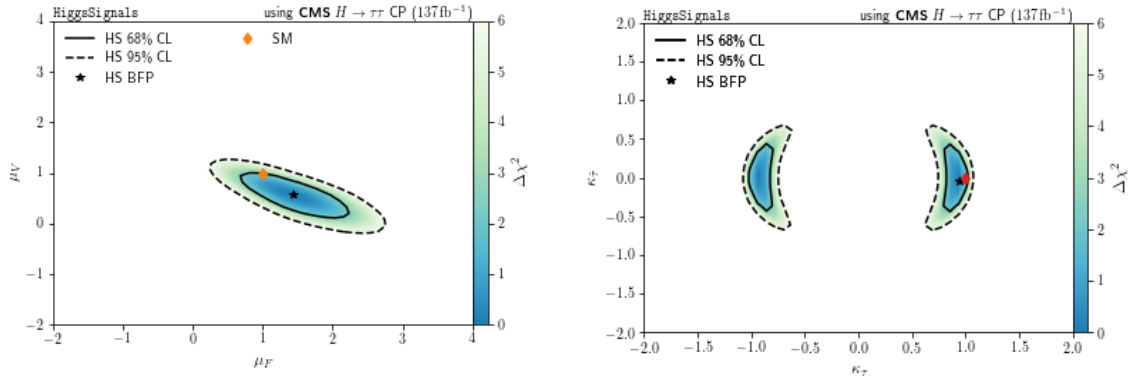


**Figure 12:** Figures taken from the public HS code, describing measurement number 13, relative to Ref. [54]. Left: reported value of  $\mu_{ggH}^{\tau\tau} = 0.59_{-0.32}^{+0.28}$ . Right: plane  $\text{sign}(k_V)c_\tau^o$  vs.  $\text{sign}(k_V)c_\tau^e$ .

is excluded at the  $1\sigma$  level. Importantly, this behavior originates from the experimental result reported in Ref. [54] itself and is not an artifact of its implementation within HS. This observation can be placed in context by comparing it with the corresponding ATLAS measurements [93], which yield  $\mu_{ggF+bbH}^{\tau\tau} = 0.89788_{-0.25638}^{+0.29101}$  and  $\mu_{ggF+bbH}^{bb} = 0.98031_{-0.36282}^{+0.37558}$ . These results are consistent with the SM expectation and do not exhibit a similar tension.

For this reason, we exclude the specific submeasurement of Ref. [54]’s  $\mu_{ggH}^{\tau\tau}$  from the  $\chi^2$  evaluation in HS. In practice, this is achieved by commenting out the  $\mu_{ggH}^{\tau\tau}$  entry in the corresponding HS dataset file [https://gitlab.com/higgsbounds/hsdataset/-/blob/main/h125/tautau\\_CP\\_LHC13\\_CMS\\_137.json?ref\\_Type=heads](https://gitlab.com/higgsbounds/hsdataset/-/blob/main/h125/tautau_CP_LHC13_CMS_137.json?ref_Type=heads). With this single submeasurement removed, the SM reference value is updated to  $\chi_{\text{SM}}^2 = 150.2$ , compared to the original value  $\chi_{\text{SM}}^2 = 152.54$ . Reapplying HS to the parameter points shown in Fig. 11 then yields the results displayed in Fig. 13, where 400 points out of the original 4096 are now found to be compatible with the HS constraints.

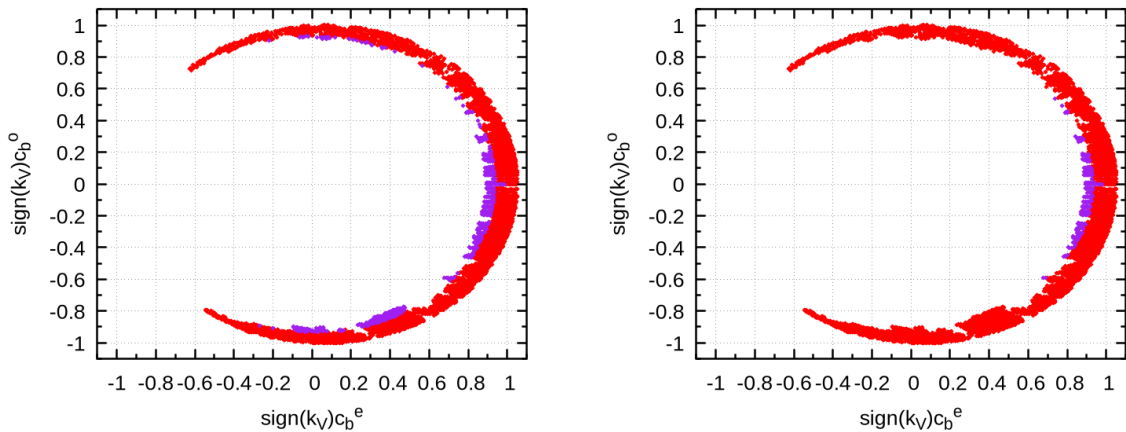


**Figure 13:** Points on the plane  $\text{sign}(k_V)c_b^o$  vs.  $\text{sign}(k_V)c_b^e$  in the Type-II C2HDM with  $h_{125} = h_2$ . Red points pass all constraints except those relative to  $\theta_\tau$ , violet points add these constraints using a modified HS: with Ref. [54] removed as a whole (left), or with only the  $\mu_{ggH}^{\tau\tau}$  measurement removed (right). The right panel is identical to the left one of Fig. 1.

## References

- [1] T. D. Lee, *A Theory of Spontaneous T Violation*, *Phys. Rev. D* **8** (1973) 1226–1239.
- [2] BABAR collaboration, B. Aubert et al., *Observation of CP violation in the  $B^0$  meson system*, *Phys. Rev. Lett.* **87** (2001) 091801, [[hep-ex/0107013](#)].
- [3] BELLE collaboration, K. Abe et al., *Observation of large CP violation in the neutral B meson system*, *Phys. Rev. Lett.* **87** (2001) 091802, [[hep-ex/0107061](#)].
- [4] S. L. Glashow and S. Weinberg, *Natural Conservation Laws for Neutral Currents*, *Phys. Rev. D* **15** (1977) 1958.
- [5] E. A. Paschos, *Diagonal Neutral Currents*, *Phys. Rev. D* **15** (1977) 1966.
- [6] I. F. Ginzburg, M. Krawczyk and P. Osland, *Two Higgs doublet models with CP violation*, in *International Workshop on Linear Colliders (LCWS 2002)*, pp. 703–706, 11, 2002, [[hep-ph/0211371](#)].
- [7] J. F. Gunion and H. E. Haber, *The CP conserving two Higgs doublet model: The Approach to the decoupling limit*, *Phys. Rev. D* **67** (2003) 075019, [[hep-ph/0207010](#)].
- [8] I. F. Ginzburg and M. Krawczyk, *Symmetries of two Higgs doublet model and CP violation*, *Phys. Rev. D* **72** (2005) 115013, [[hep-ph/0408011](#)].
- [9] A. W. El Kaffas, W. Khater, O. M. Ogreid and P. Osland, *Consistency of the two Higgs doublet model and CP violation in top production at the LHC*, *Nucl. Phys. B* **775** (2007) 45–77, [[hep-ph/0605142](#)].
- [10] A. Arhrib, E. Christova, H. Eberl and E. Ginina, *CP violation in charged Higgs production and decays in the Complex Two Higgs Doublet Model*, *JHEP* **04** (2011) 089, [[1011.6560](#)].
- [11] A. Barroso, P. M. Ferreira, R. Santos and J. P. Silva, *Probing the scalar-pseudoscalar mixing in the 125 GeV Higgs particle with current data*, *Phys. Rev. D* **86** (2012) 015022, [[1205.4247](#)].
- [12] S. Inoue, M. J. Ramsey-Musolf and Y. Zhang, *CP-violating phenomenology of flavor conserving two Higgs doublet models*, *Phys. Rev. D* **89** (2014) 115023, [[1403.4257](#)].
- [13] D. Fontes, J. C. Romão and J. P. Silva,  *$h \rightarrow Z\gamma$  in the complex two Higgs doublet model*, *JHEP* **12** (2014) 043, [[1408.2534](#)].
- [14] B. Grzadkowski, O. M. Ogreid and P. Osland, *Measuring CP violation in Two-Higgs-Doublet models in light of the LHC Higgs data*, *JHEP* **11** (2014) 084, [[1409.7265](#)].
- [15] A. W. El Kaffas, P. Osland and O. M. Ogreid, *CP violation, stability and unitarity of the two Higgs doublet model*, *Nonlin. Phenom. Complex Syst.* **10** (2007) 347–357, [[hep-ph/0702097](#)].
- [16] B. Grzadkowski and P. Osland, *Tempered Two-Higgs-Doublet Model*, *Phys. Rev. D* **82** (2010) 125026, [[0910.4068](#)].
- [17] W. Khater and P. Osland, *CP violation in top quark production at the LHC and two Higgs doublet models*, *Nucl. Phys. B* **661** (2003) 209–234, [[hep-ph/0302004](#)].
- [18] K. Cheung, J. S. Lee, E. Senaha and P.-Y. Tseng, *Confronting Higgsphysics with Electric Dipole Moments*, *JHEP* **06** (2014) 149, [[1403.4775](#)].

- [19] R. Grober, M. Muhlleitner and M. Spira, *Higgs Pair Production at NLO QCD for CP-violating Higgs Sectors*, *Nucl. Phys. B* **925** (2017) 1–27, [[1705.05314](#)].
- [20] D. Fontes, J. C. Romão, R. Santos and J. P. Silva, *Undoubtable signs of CP-violation in Higgs boson decays at the LHC run 2*, *Phys. Rev. D* **92** (2015) 055014, [[1506.06755](#)].
- [21] D. Fontes, J. C. Romão, R. Santos and J. P. Silva, *Large pseudoscalar Yukawa couplings in the complex 2HDM*, *JHEP* **06** (2015) 060, [[1502.01720](#)].
- [22] T. Abe, J. Hisano, T. Kitahara and K. Tobioka, *Gauge invariant Barr-Zee type contributions to fermionic EDMs in the two-Higgs doublet models*, *JHEP* **01** (2014) 106, [[1311.4704](#)]. [Erratum: *JHEP* 04, 161 (2016)].
- [23] C.-Y. Chen, S. Dawson and Y. Zhang, *Complementarity of LHC and EDMs for Exploring Higgs CP Violation*, *JHEP* **06** (2015) 056, [[1503.01114](#)].
- [24] C.-Y. Chen, H.-L. Li and M. Ramsey-Musolf, *CP-Violation in the Two Higgs Doublet Model: from the LHC to EDMs*, *Phys. Rev. D* **97** (2018) 015020, [[1708.00435](#)].
- [25] D. Fontes, M. Mühlleitner, J. C. Romão, R. Santos, J. P. Silva and J. Wittbrodt, *The C2HDM revisited*, *JHEP* **02** (2018) 073, [[1711.09419](#)].
- [26] E. J. Chun, J. Kim and T. Mondal, *Electron EDM and Muon anomalous magnetic moment in Two-Higgs-Doublet Models*, *JHEP* **12** (2019) 068, [[1906.00612](#)].
- [27] K. Cheung, A. Jueid, Y.-N. Mao and S. Moretti, *Two-Higgs-doublet model with soft CP violation confronting electric dipole moments and colliders*, *Phys. Rev. D* **102** (2020) 075029, [[2003.04178](#)].
- [28] M. Frank, E. G. Fuakye and M. Toharia, *Restricting the parameter space of type-II two-Higgs-doublet models with CP violation*, *Phys. Rev. D* **106** (2022) 035010, [[2112.14295](#)].
- [29] T. Biekötter, D. Fontes, M. Mühlleitner, J. C. Romão, R. Santos and J. P. Silva, *Impact of new experimental data on the C2HDM: the strong interdependence between LHC Higgs data and the electron EDM*, *JHEP* **05** (2024) 127, [[2403.02425](#)].
- [30] M. Mühlleitner, M. O. P. Sampaio, R. Santos and J. Wittbrodt, *Phenomenological Comparison of Models with Extended Higgs Sectors*, *JHEP* **08** (2017) 132, [[1703.07750](#)].
- [31] P. Basler, M. Mühlleitner and J. Wittbrodt, *The CP-Violating 2HDM in Light of a Strong First Order Electroweak Phase Transition and Implications for Higgs Pair Production*, *JHEP* **03** (2018) 061, [[1711.04097](#)].
- [32] M. Aoki, K. Hashino, D. Kaneko, S. Kanemura and M. Kubota, *Probing CP violating Higgs sectors via the precision measurement of coupling constants*, *PTEP* **2019** (2019) 053B02, [[1808.08770](#)].
- [33] P. Basler, M. Mühlleitner and J. Müller, *Electroweak Phase Transition in Non-Minimal Higgs Sectors*, *JHEP* **05** (2020) 016, [[1912.10477](#)].
- [34] X. Wang, F. P. Huang and X. Zhang, *Gravitational wave and collider signals in complex two-Higgs doublet model with dynamical CP-violation at finite temperature*, *Phys. Rev. D* **101** (2020) 015015, [[1909.02978](#)].
- [35] R. Boto, T. V. Fernandes, H. E. Haber, J. C. Romão and J. P. Silva, *Basis-independent treatment of the complex 2HDM*, *Phys. Rev. D* **101** (2020) 055023, [[2001.01430](#)].



- [36] W. Altmannshofer, S. Gori, N. Hamer and H. H. Patel, *Electron EDM in the complex two-Higgs doublet model*, *Phys. Rev. D* **102** (2020) 115042, [2009.01258].
- [37] D. Fontes and J. C. Romão, *Renormalization of the C2HDM with FeynMaster 2*, *JHEP* **06** (2021) 016, [2103.06281]. [Erratum: JHEP 12, 005 (2021)].
- [38] P. Basler, L. Biermann, M. Mühlleitner and J. Müller, *Electroweak baryogenesis in the CP-violating two-Higgs doublet model*, *Eur. Phys. J. C* **83** (2023) 57, [2108.03580].
- [39] H. Abouabid, A. Arhrib, D. Azevedo, J. E. Falaki, P. M. Ferreira, M. Mühlleitner et al., *Benchmarking di-Higgs production in various extended Higgs sector models*, *JHEP* **09** (2022) 011, [2112.12515].
- [40] D. Fontes and J. C. Romão, *The one-loop impact of a dependent mass: the role of  $m_3$  in the C2HDM*, *JHEP* **03** (2022) 144, [2201.02479].
- [41] D. Azevedo, T. Biekötter and P. M. Ferreira, *2HDM interpretations of the CMS diphoton excess at 95 GeV*, *JHEP* **11** (2023) 017, [2305.19716].
- [42] D. Gonçalves, A. Kaladharan and Y. Wu, *Gravitational waves, bubble profile, and baryon asymmetry in the complex 2HDM*, *Phys. Rev. D* **108** (2023) 075010, [2307.03224].
- [43] S. M. Barr and A. Zee, *Electric Dipole Moment of the Electron and of the Neutron*, *Phys. Rev. Lett.* **65** (1990) 21–24. [Erratum: Phys.Rev.Lett. 65, 2920 (1990)].
- [44] R. G. Leigh, S. Paban and R. M. Xu, *Electric dipole moment of electron*, *Nucl. Phys. B* **352** (1991) 45–58.
- [45] J. F. Gunion and R. Vega, *The Electron electric dipole moment for a CP violating neutral Higgs sector*, *Phys. Lett. B* **251** (1990) 157–162.
- [46] D. Chang, W.-Y. Keung and T. C. Yuan, *Two Loop Bosonic Contribution to the Electron Electric Dipole Moment*, *Phys. Rev. D* **43** (1991) R14–R16.
- [47] W. Altmannshofer, B. Assi, J. Brod, N. Hamer, J. Julio, P. Uttayarat et al., *Electron EDM and  $\Gamma(\mu \rightarrow e\gamma)$  in the 2HDM*, *JHEP* **06** (2025) 156, [2410.17313].
- [48] ACME collaboration, J. Baron et al., *Order of Magnitude Smaller Limit on the Electric Dipole Moment of the Electron*, *Science* **343** (2014) 269–272, [1310.7534].
- [49] ACME collaboration, V. Andreev et al., *Improved limit on the electric dipole moment of the electron*, *Nature* **562** (2018) 355–360.
- [50] T. S. Roussy et al., *An improved bound on the electron’s electric dipole moment*, *Science* **381** (2023) adg4084, [2212.11841].
- [51] A. C. Vutha, M. Horbatsch and E. A. Hessels, *Orientation-dependent hyperfine structure of polar molecules in a rare-gas matrix: A scheme for measuring the electron electric dipole moment*, *Phys. Rev. A* **98** (2018) 032513, [1806.06774].
- [52] M. Ardu, M. H. Rahat, N. Valori and O. Vives, *Electric Dipole Moments as indirect probes of dark sectors*, *JHEP* **11** (2024) 049, [2407.21100].
- [53] M. Aiko, M. Endo, S. Kanemura and Y. Mura, *Electroweak baryogenesis in 2HDM without EDM cancellation*, *JHEP* **07** (2025) 236, [2504.07705].
- [54] CMS collaboration, A. Tumasyan et al., *Analysis of the CP structure of the Yukawa coupling between the Higgs boson and  $\tau$  leptons in proton-proton collisions at  $\sqrt{s} = 13$  TeV*, *JHEP* **06** (2022) 012, [2110.04836].

- [55] ATLAS collaboration, G. Aad et al., *Observation of a new particle in the search for the Standard Model Higgs boson with the ATLAS detector at the LHC*, *Phys. Lett. B* **716** (2012) 1–29, [[1207.7214](#)].
- [56] CMS collaboration, S. Chatrchyan et al., *Observation of a New Boson at a Mass of 125 GeV with the CMS Experiment at the LHC*, *Phys. Lett. B* **716** (2012) 30–61, [[1207.7235](#)].
- [57] R. Boto, L. Lourenco, J. C. Romão and J. P. Silva, *Large pseudoscalar Yukawa couplings in the complex 3HDM*, *JHEP* **11** (2024) 106, [[2407.19856](#)].
- [58] F. A. de Souza, R. Boto, M. Crispim Romão, P. N. Figueiredo, J. C. Romão and J. P. Silva, *Unearthing large pseudoscalar Yukawa couplings with machine learning*, *JHEP* **07** (2025) 268, [[2505.10625](#)].
- [59] M. Feickert and B. Nachman, *A Living Review of Machine Learning for Particle Physics*, [2102.02770](#).
- [60] P. Shanahan et al., *Snowmass 2021 Computational Frontier CompF03 Topical Group Report: Machine Learning*, [2209.07559](#).
- [61] T. Plehn, A. Butter, B. Dillon, T. Heimel, C. Krause and R. Winterhalder, *Modern Machine Learning for LHC Physicists*, [2211.01421](#).
- [62] S. Caron, T. Heskes, S. Otten and B. Stienen, *Constraining the Parameters of High-Dimensional Models with Active Learning*, *Eur. Phys. J. C* **79** (2019) 944, [[1905.08628](#)].
- [63] J. Hollingsworth, M. Ratz, P. Tanedo and D. Whiteson, *Efficient sampling of constrained high-dimensional theoretical spaces with machine learning*, *Eur. Phys. J. C* **81** (2021) 1138, [[2103.06957](#)].
- [64] M. D. Goodsell and A. Joury, *Active learning BSM parameter spaces*, *Eur. Phys. J. C* **83** (2023) 268, [[2204.13950](#)].
- [65] M. A. Diaz, G. Cerro, S. Dasmahapatra and S. Moretti, *Bayesian Active Search on Parameter Space: a 95 GeV Spin-0 Resonance in the (B – L)SSM*, [2404.18653](#).
- [66] S. AbdusSalam, S. Abel and M. Crispim Romão, *Symbolic regression for beyond the standard model physics*, *Phys. Rev. D* **111** (2025) 015022, [[2405.18471](#)].
- [67] N. Batra, B. Coleppa, A. Khanna, S. K. Rai and A. Sarkar, *Constraining the 3HDM Parameter Space*, [2504.07489](#).
- [68] A. Hammad, R. Ramos, A. Chakraborty, P. Ko and S. Moretti, *Explaining Data Anomalies over the NMSSM Parameter Space with Deep Learning Techniques*, [2508.13912](#).
- [69] F. A. de Souza, M. Crispim Romão, N. F. Castro, M. Nikjoo and W. Porod, *Exploring parameter spaces with artificial intelligence and machine learning black-box optimization algorithms*, *Phys. Rev. D* **107** (2023) 035004, [[2206.09223](#)].
- [70] J. C. Romão and M. Crispim Romão, *Combining evolutionary strategies and novelty detection to go beyond the alignment limit of the Z3 3HDM*, *Phys. Rev. D* **109** (2024) 095040, [[2402.07661](#)].
- [71] H. Georgi and D. V. Nanopoulos, *Suppression of Flavor Changing Effects From Neutral Spinless Meson Exchange in Gauge Theories*, *Phys. Lett. B* **82** (1979) 95–96.
- [72] J. F. Donoghue and L. F. Li, *Properties of Charged Higgs Bosons*, *Phys. Rev. D* **19** (1979) 945.

- [73] L. Lavoura and J. P. Silva, *Fundamental CP violating quantities in a  $SU(2) \times U(1)$  model with many Higgs doublets*, *Phys. Rev. D* **50** (1994) 4619–4624, [[hep-ph/9404276](#)].
- [74] F. J. Botella and J. P. Silva, *Jarlskog - like invariants for theories with scalars and fermions*, *Phys. Rev. D* **51** (1995) 3870–3875, [[hep-ph/9411288](#)].
- [75] F. A. de Souza, N. F. Castro, M. Crispim Romão and W. Porod, *Exploring scotogenic parameter spaces and mapping uncharted dark matter phenomenology with multi-objective search algorithms*, *JHEP* **10** (2025) 116, [[2505.08862](#)].
- [76] R. Boto, J. A. C. Matos, J. C. Romão and J. P. Silva, *Surveying the complex three Higgs doublet model with Machine Learning*, [2510.02445](#).
- [77] ATLAS collaboration, G. Aad et al., *CP Properties of Higgs Boson Interactions with Top Quarks in the  $t\bar{t}H$  and  $tH$  Processes Using  $H \rightarrow \gamma\gamma$  with the ATLAS Detector*, *Phys. Rev. Lett.* **125** (2020) 061802, [[2004.04545](#)].
- [78] ATLAS collaboration, G. Aad et al., *Measurement of the CP properties of Higgs boson interactions with  $\tau$ -leptons with the ATLAS detector*, *Eur. Phys. J. C* **83** (2023) 563, [[2212.05833](#)].
- [79] N. Yamanaka, *Analysis of the Electric Dipole Moment in the R-parity Violating Supersymmetric Standard Model*, Ph.D. thesis, Osaka U., 2013. 10.1007/978-4-431-54544-6.
- [80] S. F. King, M. Muhlleitner, R. Nevzorov and K. Walz, *Exploring the CP-violating NMSSM: EDM Constraints and Phenomenology*, *Nucl. Phys. B* **901** (2015) 526–555, [[1508.03255](#)].
- [81] H. Bahl, E. Fuchs, S. Heinemeyer, J. Katzy, M. Menen, K. Peters et al., *Constraining the CP structure of Higgs-fermion couplings with a global LHC fit, the electron EDM and baryogenesis*, *Eur. Phys. J. C* **82** (2022) 604, [[2202.11753](#)].
- [82] K. G. Klimenko, *On Necessary and Sufficient Conditions for Some Higgs Potentials to Be Bounded From Below*, *Theor. Math. Phys.* **62** (1985) 58–65.
- [83] P. M. Ferreira and D. R. T. Jones, *Bounds on scalar masses in two Higgs doublet models*, *JHEP* **08** (2009) 069, [[0903.2856](#)].
- [84] I. P. Ivanov, *Minkowski space structure of the Higgs potential in 2HDM*, *Phys. Rev. D* **75** (2007) 035001, [[hep-ph/0609018](#)]. [Erratum: *Phys.Rev.D* 76, 039902 (2007)].
- [85] I. P. Ivanov and J. P. Silva, *Tree-level metastability bounds for the most general two Higgs doublet model*, *Phys. Rev. D* **92** (2015) 055017, [[1507.05100](#)].
- [86] S. Kanemura, T. Kubota and E. Takasugi, *Lee-Quigg-Thacker bounds for Higgs boson masses in a two doublet model*, *Phys. Lett. B* **313** (1993) 155–160, [[hep-ph/9303263](#)].
- [87] A. G. Akeroyd, A. Arhrib and E.-M. Naimi, *Note on tree level unitarity in the general two Higgs doublet model*, *Phys. Lett. B* **490** (2000) 119–124, [[hep-ph/0006035](#)].
- [88] I. F. Ginzburg and I. P. Ivanov, *Tree level unitarity constraints in the 2HDM with CP violation*, [[hep-ph/0312374](#)].
- [89] W. Grimus, L. Lavoura, O. M. Ogreid and P. Osland, *A Precision constraint on multi-Higgs-doublet models*, *J. Phys. G* **35** (2008) 075001, [[0711.4022](#)].
- [90] W. Grimus, L. Lavoura, O. M. Ogreid and P. Osland, *The Oblique parameters in multi-Higgs-doublet models*, *Nucl. Phys. B* **801** (2008) 81–96, [[0802.4353](#)].

- [91] GFITTER GROUP collaboration, M. Baak, J. Cúth, J. Haller, A. Hoecker, R. Kogler, K. Mönig et al., *The global electroweak fit at NNLO and prospects for the LHC and ILC*, *Eur. Phys. J. C* **74** (2014) 3046, [[1407.3792](#)].
- [92] ATLAS collaboration, G. Aad et al., *Combined measurements of Higgs boson production and decay using up to 80 fb<sup>-1</sup> of proton-proton collision data at  $\sqrt{s} = 13$  TeV collected with the ATLAS experiment*, *Phys. Rev. D* **101** (2020) 012002, [[1909.02845](#)].
- [93] ATLAS collaboration, G. Aad et al., *A detailed map of Higgs boson interactions by the ATLAS experiment ten years after the discovery*, *Nature* **607** (2022) 52–59, [[2207.00092](#)]. [Erratum: *Nature* 612, E24 (2022)].
- [94] CMS collaboration, A. Tumasyan et al., *A portrait of the Higgs boson by the CMS experiment ten years after the discovery.*, *Nature* **607** (2022) 60–68, [[2207.00043](#)]. [Erratum: *Nature* 623, (2023)].
- [95] H. Bahl, T. Biekötter, S. Heinemeyer, C. Li, S. Paasch, G. Weiglein et al., *HiggsTools: BSM scalar phenomenology with new versions of HiggsBounds and HiggsSignals*, *Comput. Phys. Commun.* **291** (2023) 108803, [[2210.09332](#)].
- [96] F. Borzumati and C. Greub, *2HDMs predictions for anti-B  $\rightarrow$  X(s) gamma in NLO QCD*, *Phys. Rev. D* **58** (1998) 074004, [[hep-ph/9802391](#)].
- [97] HFLAV collaboration, Y. S. Amhis et al., *Averages of b-hadron, c-hadron, and  $\tau$ -lepton properties as of 2018*, *Eur. Phys. J. C* **81** (2021) 226, [[1909.12524](#)].
- [98] O. Deschamps, S. Descotes-Genon, S. Monteil, V. Niess, S. T’Jampens and V. Tisserand, *The Two Higgs Doublet of Type II facing flavour physics data*, *Phys. Rev. D* **82** (2010) 073012, [[0907.5135](#)].
- [99] F. Mahmoudi and O. Stal, *Flavor constraints on the two-Higgs-doublet model with general Yukawa couplings*, *Phys. Rev. D* **81** (2010) 035016, [[0907.1791](#)].
- [100] T. Hermann, M. Misiak and M. Steinhauser,  *$\bar{B} \rightarrow X_s \gamma$  in the Two Higgs Doublet Model up to Next-to-Next-to-Leading Order in QCD*, *JHEP* **11** (2012) 036, [[1208.2788](#)].
- [101] M. Misiak et al., *Updated NNLO QCD predictions for the weak radiative B-meson decays*, *Phys. Rev. Lett.* **114** (2015) 221801, [[1503.01789](#)].
- [102] M. Misiak and M. Steinhauser, *Weak radiative decays of the B meson and bounds on  $M_{H^\pm}$  in the Two-Higgs-Doublet Model*, *Eur. Phys. J. C* **77** (2017) 201, [[1702.04571](#)].
- [103] J. Haller, A. Hoecker, R. Kogler, K. Mönig, T. Peiffer and J. Stelzer, *Update of the global electroweak fit and constraints on two-Higgs-doublet models*, *Eur. Phys. J. C* **78** (2018) 675, [[1803.01853](#)].
- [104] H. E. Haber and D. O’Neil, *Basis-independent methods for the two-Higgs-doublet model III: The CP-conserving limit, custodial symmetry, and the oblique parameters S, T, U*, *Phys. Rev. D* **83** (2011) 055017, [[1011.6188](#)].
- [105] N. Hansen and A. Ostermeier, *Completely derandomized self-adaptation in evolution strategies*, *Evolutionary Computation* **9** (2001) 159–195.
- [106] N. Hansen, *The cma evolution strategy: A tutorial*, 2023.
- [107] M. Goldstein and A. Dengel, *Histogram-based outlier score (hbos): A fast unsupervised anomaly detection algorithm*, 09, 2012.

- [108] M. Mühlleitner, M. O. P. Sampaio, R. Santos and J. Wittbrodt, *ScannerS: parameter scans in extended scalar sectors*, *Eur. Phys. J. C* **82** (2022) 198, [[2007.02985](#)].
- [109] CMS collaboration, A. M. Sirunyan et al., *Search for additional neutral MSSM Higgs bosons in the  $\tau\tau$  final state in proton-proton collisions at  $\sqrt{s} = 13$  TeV*, *JHEP* **09** (2018) 007, [[1803.06553](#)].
- [110] CMS collaboration, A. Tumasyan et al., *Searches for additional Higgs bosons and for vector leptoquarks in  $\tau\tau$  final states in proton-proton collisions at  $\sqrt{s} = 13$  TeV*, *JHEP* **07** (2023) 073, [[2208.02717](#)].
- [111] ATLAS collaboration, G. Aad et al., *Search for heavy resonances decaying into a Z or W boson and a Higgs boson in final states with leptons and b-jets in  $139 \text{ fb}^{-1}$  of pp collisions at  $\sqrt{s} = 13$  TeV with the ATLAS detector*, *JHEP* **06** (2023) 016, [[2207.00230](#)].
- [112] C. Peset, A. Pineda and J. Segovia, *The charm/bottom quark mass from heavy quarkonium at  $N^3\text{LO}$* , *JHEP* **09** (2018) 167, [[1806.05197](#)].
- [113] A. Denner, S. Dittmaier, M. Grazzini, R. V. Harlander, R. S. Thorne, M. Spira et al., *Standard Model input parameters for Higgs physics*, .
- [114] ATLAS collaboration, M. Aaboud et al., *Combination of searches for heavy resonances decaying into bosonic and leptonic final states using  $36 \text{ fb}^{-1}$  of proton-proton collision data at  $\sqrt{s} = 13$  TeV with the ATLAS detector*, *Phys. Rev. D* **98** (2018) 052008, [[1808.02380](#)].
- [115] ATLAS collaboration, G. Aad et al., *Search for heavy resonances decaying into a pair of Z bosons in the  $\ell^+\ell^-\ell'^+\ell'^-$  and  $\ell^+\ell^-\nu\bar{\nu}$  final states using  $139 \text{ fb}^{-1}$  of proton-proton collisions at  $\sqrt{s} = 13$  TeV with the ATLAS detector*, *Eur. Phys. J. C* **81** (2021) 332, [[2009.14791](#)].
- [116] ATLAS collaboration, *Search for resonant and non-resonant Higgs boson pair production in the  $b\bar{b}\tau^+\tau^-$  decay channel using 13 TeV pp collision data from the ATLAS detector*, .
- [117] S. Lee, A. Hammad, D. Kim and J. Song, *Intrinsic Properties of Large CP Violation in the Complex Two-Higgs-Doublet Model*, [2512.17002](#).